IRAQI JOURNAL OF APPLIED PHYSICS LETTERS

Iraqi Journal of Applied Physics Letters (IJAPLett) is a scientific periodical sponsored and published by the Iraqi Society for Alternative and Renewable Energy Sources and Techniques (I.S.A.R.E.S.T.).

The Editorial Board is responsible for the scientific content and other editorial matters relating to the Journal. Manuscripts submitted are first screened by the editors; those on subject matters within the scope of the IJAPLett are sent to an expert referee for evaluation and may be sent to a second reviewer if necessary. This screening process helps to assure an appropriate focus as well as high scientific quality of the Journal. The IJAPLett welcomes submission of papers and letters in applied physics and related fields of science, engineering and technology. They should have something in common with what we now publish on inanimate materials and processes therein: structures, transport, physical, electrical, dielectric, magnetic, and optical properties. Our basic criterion stated below will continue to apply: papers must contain science, especially physics, and there must be an application. We advise authors submitting papers to suggest the names of at least two possible reviewers, with full information on addresses, phone and email. Suggestions of reviewers are welcome regardless of the subject.

SPONSORED AND PUBLISHED BY

THE IRAQI SOCIETY FOR ALTERNATIVE AND RENEWABLE ENERGY SOURCES AND TECHNIQUES (I.S.A.R.E.S.T.)

PRINTED IN IRAQ **ISSN 1999-656X**

" INSTRUCTIONS TO AUTHORS "

CONTRIBUTIONS

Contributions to be published in this journal should be original research works, i.e., those not already published or submitted for publication elsewhere, individual papers or letters to editor.

SUBMISSION OF MANUSCRIPTS

Manuscripts should be submitted to the editor at the mailing address:

Iraqi Journal of Applied Physics Letters
Editorial Board
P. O. Box 55259, Baghdad 12001, IRAQ
ijaplett@ijap.org , editor@ijap.org

MANUSCRIPTS

Two hard copies with soft copy on a compact disc (CD) should be submitted to Editor in the following configuration:

- Double-spaced one-side A4 size with 2.5 cm margins of all sides
- Times New Roman font (16pt bold for title, 14pt bold for names, 12pt bold for headings, 12pt regular for text)
- Letters should not exceed 10 pages.
- Manuscripts presented in English only are accepted.
- English abstract not exceed 150 words
- 4 keywords (at least) should be maintained on (PACS preferred)
- Author(s) should express all quantities in SI units
- Equations should be written in equation form (*italic* and symbolic)
- Figures and Tables should be separated from text
- Figures and diagrams can be submitted in colors for assessment and they will be returned to authors after provide printable copies
- Charts should be indicated by the software used for
- Only original or high-resolution scanner photos are accepted
- For electronic submission, articles should be formatted with MS-Word software.

AUTHOR NAMES AND AFFILIATIONS

It is IJAPLett policy that all those who have participated significantly in the technical aspects of a paper be recognized as co-authors or cited in the acknowledgments. In the case of a paper with more than one author, correspondence concerning the paper will be sent to the first author unless staff is advised otherwise.
Author name should consist of first name, middle initial, last name. The author affiliation should consist of the following, as applicable, in the order noted:
- Company or college (with department name or company division)
- Postal address
- City, state, zip code, country
- Telephone, and e-mail

REFERENCES

The references should be brought at the end of the article, and numbered in the order of their appearance in the paper. The reference list should be cited in accordance with the following examples:

[1] X. Ning and M.R. Lovell, "On the Sliding Friction Characteristics of Unidirectional Continuous FRP Composites", *ASME J. Tribol.*, 124(1) (2002) 5-13.
[2] M. Barnes, "Stresses in Solenoids", *J. Appl. Phys.*, 48(5) (2001) 2000–2008.
[3] J. Jones, "Contact Mechanics", Cambridge University Press (Cambridge, UK) (2000), Ch.6, p.56.
[4] Y. Lee, S.A. Korpela and R. Horne, "Structure of Multi-Cellular Natural Convection in a Tall Vertical Annulus", Proc. 7th International Heat Transfer Conference, U. Grigul et al., eds., Hemisphere (Washington DC), 2 (1982) 221–226.
[5] M. Hashish, "Waterjet Technology Development", High Pressure Technology, PVP-Vol. 406 (2000), 135-140.
[6] D.W. Watson, "Thermodynamic Analysis", ASME Paper No. 97-GT-288 (1997).
[7] C.Y. Tung, "Evaporative Heat Transfer in the Contact Line of a Mixture", Ph.D. thesis, Rensselaer Polytechnic Institute, Troy, NY (1982).

PROOFS

Authors will receive proofs of papers and are requested to return one corrected hard copy with a WORD copy on a compact disc (CD). New materials inserted in the original text without Editor permission may cause rejection of paper.

COPYRIGHT FORM

Author(s) will be asked to transfer copyrights of the article to the Journal soon after acceptance of it. This will ensure the widest possible dissemination of information.

OFFPRINTS

Authors will receive offprints free of charge and any additional offprints can be ordered.

SUBSCRIPTION AND ORDERS

Annual fees (4 issues per year) of subscription are:

- 50 US$ for individuals inside Iraq.
- 100 US$ for establishments inside Iraq.
- 100 US$ for individuals abroad.
- 200 US$ for establishments abroad.

Fees are reduced by 25% for I.S.A.R.E.S.T. members. Orders of issues can be submitted by contacting the editor-in-chief or editorial office at **subscription@ijap.org** to maintain the address of issue delivery and payment way.

Aseel A. AlSharify

Department of Laser and Optoelectronics Engineering, University of Technology, Baghdad, Iraq

Design and Simulation of DPSS Laser with SHG for Material Processing

In the present work, multilayer reflection coating analysis has been employed for design and simulating diode-pumped solid state (DPSS) laser system with second harmonic generation (SHG) using composite crystal (DPM010X). It was found that the optical reflection greatly depends on the refractive index, optical thickness and number of anti-reflection coating layers used. The calculated refractive index was found to be 1.949 for phase matched angle of 23.2° for the KTP non-linear crystal.

***Keywords*:** DPSSL, SHG, KTP, Nonlinear crystal, Optical pumping
Received: 6 November 2008, Revised: 8 December 2008, Accepted 15 December 2008

1. Introduction

Diode-pumped solid state (DPSS) lasers are the ideal laser tools for machining, material processing, spectroscopy, wafer inspection, light show, medical diagnostics and other applications. The DPM composite crystals, which combine the vanadate Nd:YVO_4 and KTP, are mainly used for low power applications, for example, green laser pointers [1]. Here are some systems that will get you some green light without either expensive crystals or the need for complex mounting and infinite alignment fiddling, as shown in the Fig. (1), where a hybrid (also called composite) vanadate-KTP crystal, and a 100 to 500mW, 808nm pump diode are needed. The resulting laser should be capable of 5-10mW of green light with DPM010X composite crystal [1].

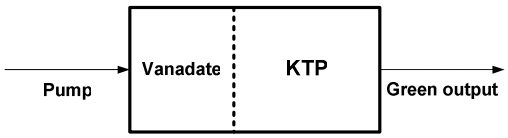

Fig. (1) Schematic diagram of the DPM1101 composite crystal [1]

2. Theory

Second harmonic generation (SHG) occurs when an intense light beam of angular frequency ω passing through an appropriate crystal (e.g. KTP) and generates a light beam of double the frequency (ω_2). If E is the electric field in the light wave, then the induced polarization P becomes a function of E and can be written as

$$P = \varepsilon_0 \chi_1 E_0 \sin(\omega t) - \frac{1}{2}\varepsilon_0 \chi_2 E_0 \cos(2\omega t) + \frac{1}{2}\varepsilon_0 \chi_3 E_0 \quad (1)$$

where χ_1, χ_2 and χ_3 are the linear, second-order and third-order susceptibilities

SHG is based on a finite χ_2 coefficient in which the effect of χ_3 is negligible. The first term is the fundamental, second is the second harmonic and third is the dc term. The second harmonic (2ω oscillation of local dipole moments generates secondary second harmonic (2ω) waves in the crystal as shown in Fig. (2).

However, the crystal will normally possess different refractive indices $n(\omega)$ and $n(2\omega)$ for frequencies ω and 2ω. The condition that the second harmonic waves must travel with the same phase velocity as the fundamental wave to constitute a second harmonic beam is called phase matching and requires $n(\omega)=n(2\omega)$. One method is to use a birefringent crystal as these have two refractive indices: ordinary index n_o and extraordinary index n_e. Suppose that along a certain crystal direction at an angle θ to the optic axis, $n_e(2\omega)$ at the second harmonic is the same as $n_o(\omega)$ at the fundamental frequency: $n_e(2\omega)=n_o(\omega)$. This is called index matching and the angle θ is the phase matching angle. To separate the second harmonic beam from the fundamental beam, something like a diffraction grating, a prism or an optical filter (such as anti reflection coating) will have to be used at the output as [2]. The optical matrix approach was employed for N-layer design of antireflection coating the main idea of this method is matching the E and H fields of the incident light on the interfaces of the multilayer optical coatings. The matrix relation defining the N-layer antireflection problem is given by [8]

$$\begin{bmatrix} B \\ C \end{bmatrix} = \prod_{q_i=1}^{m} \begin{bmatrix} \cos\delta_q & i\sin\frac{\delta_q}{n_q} \\ in_q \sin\delta_q & \cos\delta_q \end{bmatrix} \begin{bmatrix} 1 \\ n_s \end{bmatrix} \quad (2)$$

where B and C are total electric and magnetic field amplitudes of light propagation in the medium. Thus optical admittance is given by the ratio

$$Y = \frac{C}{B} \quad (3)$$

As n is the refractive index of the layer, then the phase thickness (δ) is given by

$$\delta = \frac{2\pi n d_q}{\lambda} \quad (4)$$

With the physical thickness of the layer being d_q, then the reflection coefficient r and the reflectivity R are respectively given by [8]

$$R = r \times r^* \quad (5)$$

where r is the reflectance

$$r = \frac{n_0 - Y}{n_0 + Y} \quad (6)$$

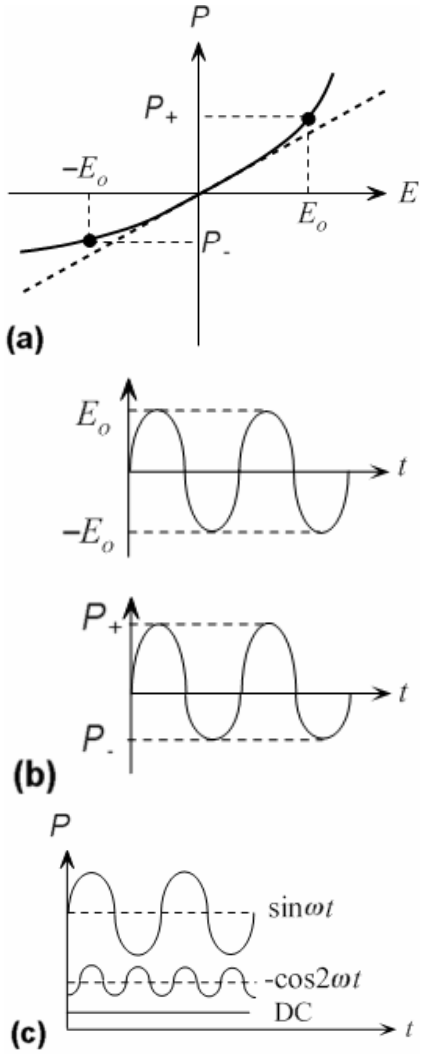

Fig. (2) Induced polarization *vs.* optical field for a nonlinear medium (a), Sinusoidal optical field oscillations between E_0 result in polarization oscillations between P_+ and P_- (b), The polarization oscillation can be represented by sinusoidal oscillations at angular (c)

3. Experiment

DPM1101 composite crystal in DPSS laser system has been chosen for designing the required model. The use of hybrid or composite crystals represents by far the easiest way to construct a low power green DPSS laser. They virtually eliminate fiddling as a pastime since the HR, Nd:YVO_4 (vanadate), KTP, and OC mirrors are all permanently aligned. For many applications, no additional optics is required. Such systems are used mainly for SHG, which involve two fundamental mode photons [9].

The dimensions of DPM0101 crystal is approximately 1x1x2.5mm. Vanadate doping and thickness: As well, the Vanadate doping is probably 3% and the thickness is 0.5mm. The main features and optical properties of vanadate are:

1- Low lasing threshold and high slope efficiency
2- Large stimulated emission cross-section at lasing wavelength
3- High absorption over a wide pumping wavelength bandwidth
4- Optically uniaxial and large birefringence emits polarized laser. Its fluorescence spectra curves are shown below in Fig. (3) [3]

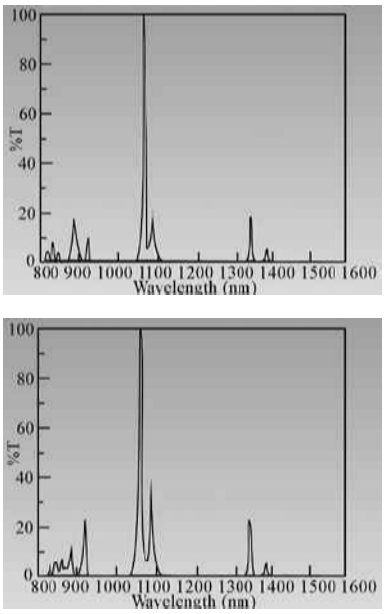

Fig. (3) Fluorescence spectra of the vanadate

Because of its large stimulated emission cross section at 1.34mm, Nd:YVO_4 is also an efficient laser crystal for diode laser-pumped 1.3mm laser [3].

By using the compact design of Nd:YVO_4+KTP crystals, high power green or red light output can be generated in a diode laser pumped Nd:YVO_4 laser and the optical properties of the vanadate are shown in table (1) [4].

- HR mirror: The coating is on the rear face of the vanadate and is HT at 808nm and HR @1064nm

KTP: The KTP is cut to provide the critical Type (2) phase matching for the 1064nm to 532nm conversion and the output 532nm light will be polarized at +45 or -45 degrees as usual. The shape of the KTP matches the vanadate and its optical properties are listed on the table (2).

Table (1) optical properties of the vanadate [4]

Lasing wavelengths	914nm, 1064 nm, 1342 nm
Crystal class	positive uniaxial, $n_o=n_a=n_b$, $n_e=n_c$
Sellmeier equation (for pure YVO_4 crystals): $n_o^2=3.77834+0.069736/(\lambda^2 - 0.04724) - 0.0108133\lambda^2$ $n_e^2=4.59905+0.110534/(\lambda^2 - 0.04813) - 0.0122676\lambda^2$	
Thermal optical coefficient:	$dn_a/dT=8.5\times10^{-6}$/K, $dn_c/dT=3.0\times10^{-6}$/K
Stimulated emission cross-section	$25.0\times10^{-19}cm^2$, @1064nm
Fluorescent lifetime	90μs (about 50μs for 2atm% Nd doped) @808nm
Absorption coefficient	$31.4cm^{-1}$ @808nm
Absorption length	0.32mm @808nm
Diode pumped optical-to-optical efficiency	>60%

Table (2) optical properties of the KTP crystal [4]

Transmitting range	350nm~4500nm			
Refractive indices		n_x	n_y	n_z
	1064nm	1.7400	1.7469	1.8304
	532nm	1.7787	1.7924	1.8873
Thermal optical coefficient:	$dn_x/dT=1.1\times10^{-5}$/°C $dn_y/dT=1.3\times10^{-5}$/°C $dn_z/dT=1.6\times10^{-5}$/°C			
Stimulated emission cross-section	$25.0\times10^{-19}cm^2$, @1064nm			
Absorption coefficient	a<1%/cm @1064nm and 532nm			

The refractive index of the SHG was measured by using equation below:

$$n_{2\omega}^{o} = \frac{1}{2}\left(n_{\omega}^{o} + n_{\omega}^{e}\right) \quad (7)$$

- OC mirror: The coating on the front face of the KTP is HR at 1064nm and AR at 532nm. Pump power for the low power DPM crystal is suggested to be less than 300mW, and the generated green output power could be less than 10mW.

The simulation of the reflection in MATLAB have been the main assignment of this work. The reflectivity of both rear and output coupler mirror have been simulated with multilayer antireflection coating after choosing the proper material for both high and low index of reflection which should have suitable absorption, good adhesion, low stress, hardness, low cost and easy preparation. The program optimize at λ_0=500nm central wavelength for visible and near infrared spectral region. The parameters of antireflection are optical thickness for each layer and refractive index for each layer coating and substrate [5]

4. Results and Discussion

Reflection was taken as function of the wavelength for different coating materials for both rear and coupling mirror, as shown in the two parts below. Figures (4-11) shows the simulated results of reflection as a function of wavelength for different low and high refractive index of materials used for coating layers for two different values of optical thickness.

Part 1: Rear mirror

In this part, the Nd:YVO_4 was taken as substrate material with refractive index of 1.9573 and reflection has been simulated with central wavelength (500nm) in the range from visible to NIR in multilayer anti-reflection technique.

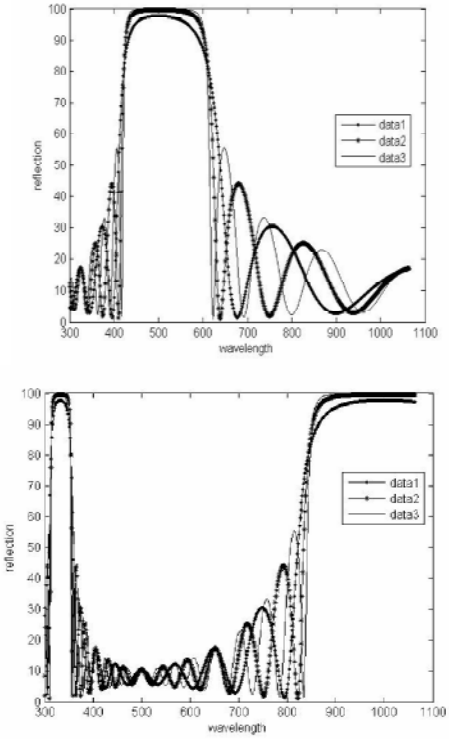

Fig. (4) Reflection as function of wavelength for ZnS as high index and MgF_2 as low index coating materials. Simulated figures with optical thickness of 0.25 (above) and 0.5 (above) for both high and low coating layers, respectively

Part 2: Output coupler mirror

In this part, the KTP birefringent crystal was taken as substrate material with measured refractive index of 1.949 and reflection has been simulated with central wavelength (500nm) in the range from visible to NIR in multilayer anti-reflection technique.

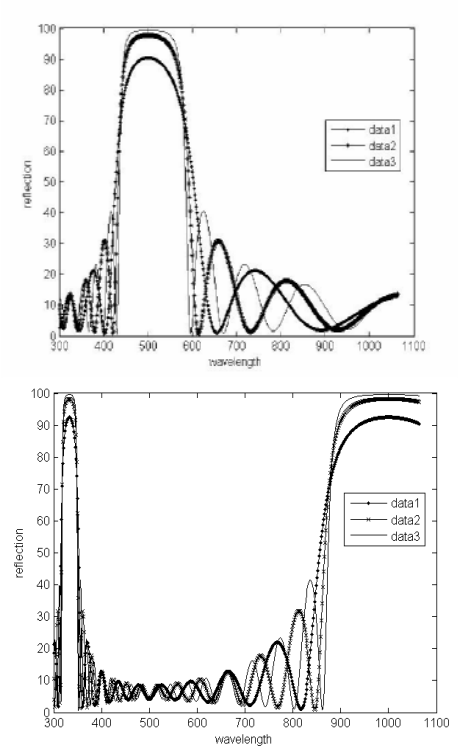

Fig. (5) Same as Fig. (4) but for SiO as high index and MgF_2 as low index coating materials. Simulated figures with optical thickness of 0.25 (above) and 0.5 (above) for both high and low coating layers, respectively

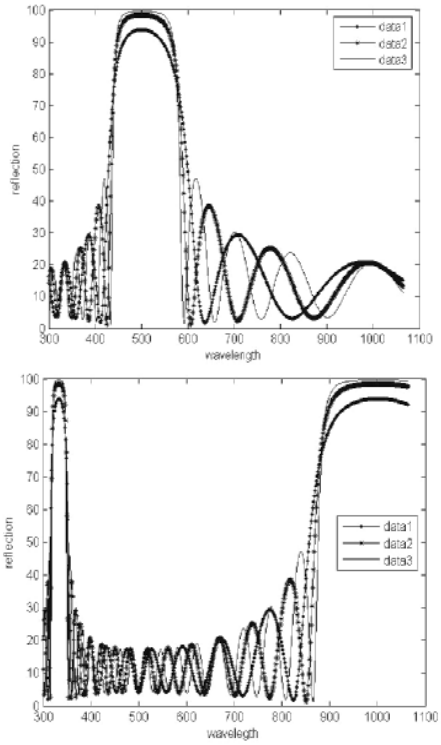

Fig. (7) Same as Fig. (4) but for PbF_3 as high index and NdF_3 as low index coating materials. Simulated figures with optical thickness of 0.25 (above) and 0.5 (above) for both high and low coating layers, respectively

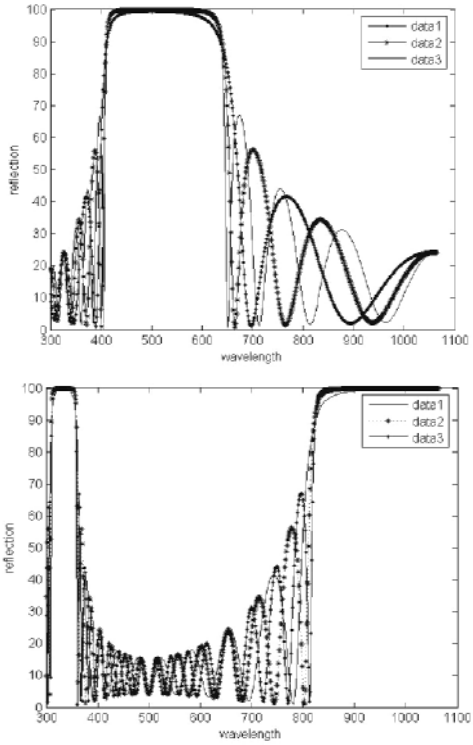

Fig. (6) Same as Fig. (4) but for ZnSe as high index and NaF as low index coating materials. Simulated figures with optical thickness of 0.25 (above) and 0.5 (above) for both high and low coating layers, respectively

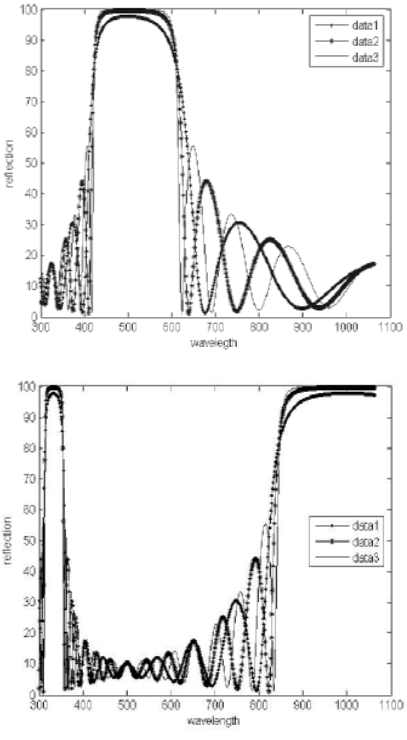

Fig. (8) Same as Fig. (4) but for ZnS as high index and MgF_2 as low index coating materials. Simulated figures with optical thickness of 0.25 (above) and 0.5 (above) for both high and low coating layers, respectively

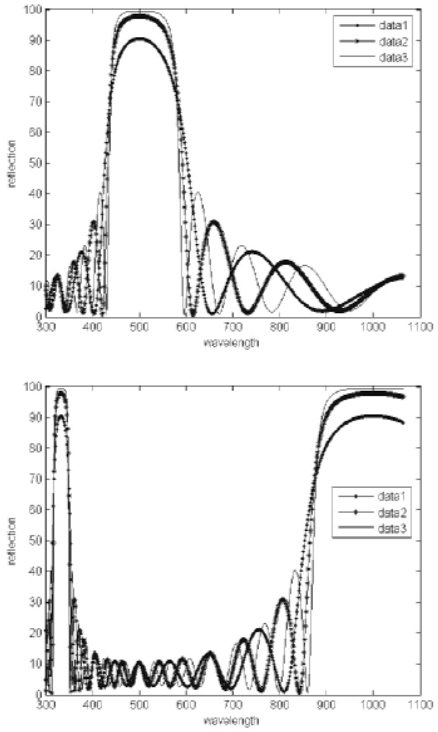

Fig. (9) Same as Fig. (4) but for SiO as high index and MgF_2 as low index coating materials. Simulated figures with optical thickness of 0.25 (above) and 0.5 (above) for both high and low coating layers, respectively

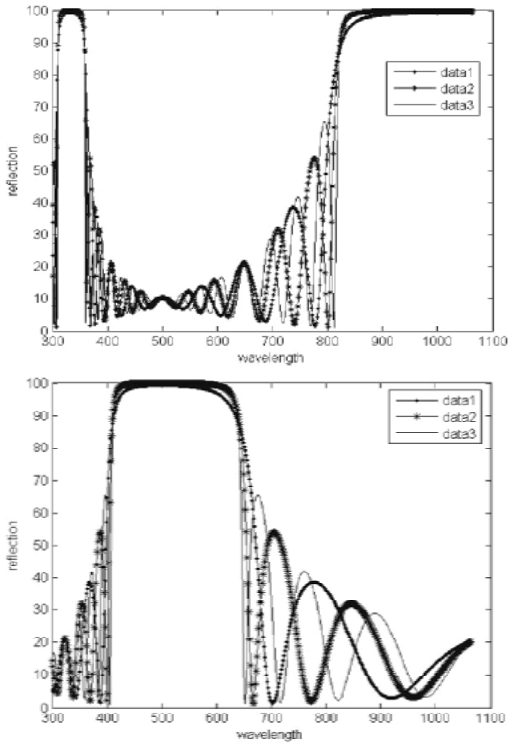

Fig. (10) Same as Fig. (4) but for ZnSe as high index and NaF as low index coating materials. Simulated figures with optical thickness of 0.25 (above) and 0.5 (above) for both high and low coating layers, respectively

In all simulated figures, *N* values strongly affected the reflectivity. Increasing *N* is a proper choice to reach the required situation of the rear mirror to be HR for the 1064nm and 532nm and HT for the 808nm [5].

This can be taken with *N*=8, as shown in figures of part 1 (data 3 curve), and from the figures of the two parts, clear differences are seen when comparing them to those resulted from the change of *N*-value. Also, there is much difference in the reflectivity behavior resulted from changing optical thickness of the anti-reflection coating. This has a limiting effect on important design requirements.

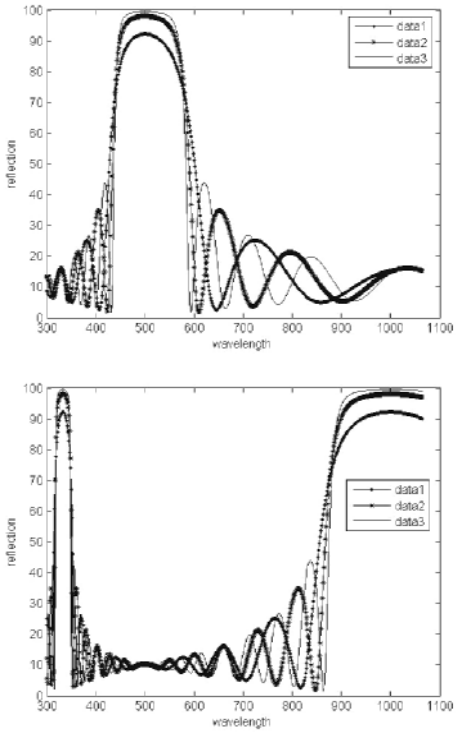

Fig. (11) Same as Fig. (4) but for PbF_2 as high index and NdF_3 as low index coating materials. Simulated figures with optical thickness of 0.25 (above) and 0.5 (above) for both high and low coating layers, respectively

Accordingly, an optical thickness value of 0.5 seems the suitable value in this work. Finally, the proper choice for the antireflection layer material is critical point because its refractive index affects reflectivity, as well as limits the lifetime of the design due to several properties, such as stress, hardness, ability to survive in different environments, cost and preparation ability.

5. Conclusion

From these results, it can be said that the best choice for the *N*-value is 10 with 0.5 optical layer thickness by which the design reaches its optimum and the SiO/MgF_2 is the best, but as ZnS and MgF_2 is much more available, lower in cost, easy in preparation and make design nearly

approaches what needed, they were suitable for the design presented in this work.

References

[1] Sam's Laser FAQ, Copyright © 1994-2008, Samuel M. Goldwasser, All Rights Reserved.

[2] Illustrated Dictionary of Important Terms and Effects in Optoelectronics and Photonics (©1999 S.O. Kasap)

[3] M.M. Fejer, G.A. Magel, D.H. Jundt, R.L. Byer, *IEEE J. Quantum Electron.*, QE-28 (1992) 2631–2654.

[4] R. Dabu, C. Fenic, A. Stratan, *Optica Applicata*, Vol. XXVI, No.3, (1996) 171–183.

[5] H.A. Macleod, **"Thin Film Optical Filters"**, 2nd edition (2001), printed in UK, Ltd., Bristol.

[6] H.E. Selhofer and R. Linsbod, *Appl. Opt.*, vol. 41 (2002) 756.

[7] J.M. Bennett et al., *Appl. Opt.*,vol. 28 (1989) 3303.

[8] H.A. Macleod, **"Thin Film Optical Filters"**, 2nd edition (2001), printed in UK, Ltd., Bristol.

[9] M. Lipinski, S. Kluska, H. Czternastek, P. Zieba, *Polish J. Mater. Sci.,* 24(4) (2006).

István Mészáros
Ali S. Mahmood

Department of Materials Science and Engineering, Budapest University of Technology and Economics, Budapest, Hungary

Complex Magnetic Investigation of Ferritic Stainless Steel

Magnetic Barkhausen noise measurement (MBN) is a relatively new non-destructive detection technique. Its working principle is based on Barkhausen discontinuities or noise when a ferromagnetic material is subjected to a varying magnetic field. MBN is being used to characterise the stress state of a ferritic stainless steel (AISI 430). Other magnetic parameters such as saturation induction (B_{Max}), remnant induction (B_R), coercive field (H_C) and maximal relative permeability (P_{Max}) derived from the hysteresis loop have also been used to support the results achieved using MBN. Microstructural changes due to cold working and heat treatments were characterized by the applied magnetic measurements. The MBN technique was proved to be a useful non-destructive and quantitative method for microstuctural investigation of the investigated ferritic stainless steel.

Keywords: Barkhausen noise, Ferritic stainless steel, Magnetic characterization
Received: 21 October 2008, Revised: 20 November, Accepted 27 November 2008

1. Introduction

High stress corrosion resistance and relatively low production costs are the main reasons for the increasing applications of AISI 430 ferritic stainless steels [1]. But problems such as loss of ductility and toughness when exposed to elevated temperatures, for instance during welding, is a main concern [2]. The use of a non-destructive evaluation technique to characterise the post-welding microstructural state of a material, could be of use in determining the optimal levels of heat input and welding speeds.

For characterisation, ferritic stainless steel (AISI 430) samples were plastically deformed and heat treated to various degrees and measured using Barkhausen sensing techniques. In a ferromagnetic material, Barkhausen noise (BN) is generated by the discontinuous movement of irreversible domains walls. This movement can be induced by applying a time varying magnetic field across the sample. This noise can be detected in the form of voltage pulses which are induced in a coil placed near the surface of the material. Magnetic Barkhausen noise (MBN) results from the irreversible displacement of domain walls. The applied mechanical stresses can increase the magnetic anisotropy of the material and can modify the domain wall mobility. Therefore, mechanical stresses can affect the magnetic Barkhausen noise.

Barkhausen noise can also be affected by pinning sites which act as barriers to domain movement. Pinning sites are attributed to various physical parameters such as grain boundaries, voids, inclusions and dislocations.

Amongst the wide range of techniques available for NDT evaluation of stresses, magnetic Barkhausen noise measurement has become very popular for stress analysis. Macroscopic magnetic properties such as differential permeability are well known to be stress-dependent [3]. The stress-dependence of differential permeability carries through to micro-scale effects to cause MBN also to be stress-dependent [4]. For detailed structural investigation of stainless steels several sophisticated electron microscopic techniques are available [5] but these techniques require destructive specimen preparation in contrast to the magnetic methods.

2. Experiment

Flat specimens have been cut from a sheet of AISI 430. The as-received chemical composition of the material included 14.19% Cr, 0.9% Mn, 84.91% Fe. These samples were deformed to various degrees of strain within the plastic range (i.e. from the yield point of the material to the ultimate tensile strength point.). Standardised test specimen dimensions (120mm x 10mm x 1.5mm) were used, and strain was measured using an extensometer with a gauge length of 50mm. Tensile tests were completed on seven samples to determine yield point and ultimate tensile strength of the specimens.

Samples plastically strained to 17.5% were subjected to annealing heat treatment for the purpose of stress relief. Heat treatments were completed for 100ºC to 1100ºC with a soaking time of 30 minutes. Samples removed from the furnace were air-cooled.

Seven specimens were elongated at each plastic strain percentage. Five measurements of each measurement technique were completed on each specimen across the surface. The standard deviation of the results from each specimen was then calculated using conventional formulae.

4. Applied Measuring Techniques

Magnetic Barkhausen noise (MBN). The magnetic Barkhausen noise utilised a sinusoidal (10 Hz) exciting magnetic field produced by a function generator and a power amplifier. The applied measuring head contained a U-shaped magnetising coil and a pick-up coil, which is perpendicular to the surface of the specimen. The signal of the pick-up coil was processed by a 0.3 kHz-38 kHz band pass filter and amplified with a gain of 50. A commercial data acquisition device with a sampling rate of 600kS/s was utilised and special software was used for processing the noise signal. The maximum magnetic field induction of the excitation was 2 mT. The Root Mean Square (RMS) value of the noise signal was determined and was used to characterise the microstructural state of the material.

A complex magnetic property analyzer was developed at the Department of Materials Science and Engineering of the BUTE. The magnetic hysteresis loop was measured by using sinusoidal (0.1 Hz) exciting magnetic field produced by a function generator and a power amplifier. The applied measuring head contains a "U" shaped laminated Fe-Si iron core with a magnetizing and a pick-up coil. The current and the voltage signals were measured by a data acquisition card. The number of measured points in a magnetizing cycle was 1000. The applied maximal excitation field strength was 5600 A/m. Saturation induction (B_{Max}), remnant induction (B_R), coercive field (H_C) and maximal relative permeability (P_{Max}) were derived from the hysteresis loop.

Microhardness. Vickers hardness (HV) measurements were completed using a Buehler MMT-3 digital microhardness tester. All tests were completed using a load of 2000 gf (19614mN).

Microstructural analysis. For microstructural examination, the etching of the ferritic AISI 430 stainless steel was carried out using swab etching with a solution of HCL, HNO_3 and H_2O with a ratio of 1:1:1. The etching time varied between 4–8 minutes. The revealed microstructures will be shown later in figures 6-a, and 6-b.

4. Results and Discussion

The dependence of MBN (RMS), the coercivity and Vickers hardness on the deformation of AISI 430 ferritic stainless steel is shown in figures (1) and (2).

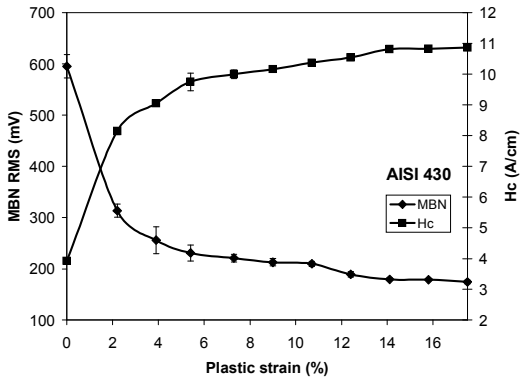

Fig. (1) Dependence of MBN and coercivity on percentage plastic strain for AISI 430

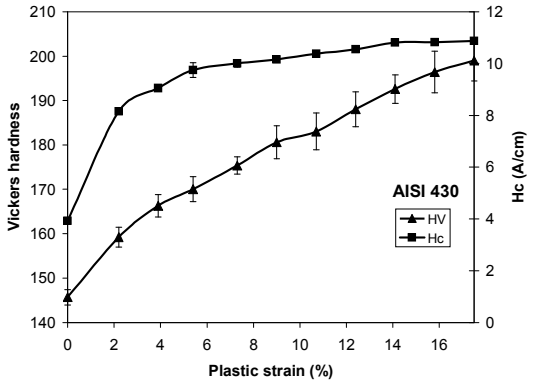

Fig. (2) Dependence of hardness and coercivity on percentage plastic strain for AISI 430

It can be seen at the lowest level of plastic strain 0% (as-received condition), where no permanent deformation of the material has occurred, the MBN is seen to be its highest (Fig. 1). With increased straining, MBN continuously reduces while the coercivity and the hardness increases (Fig. 2).

It is known that plastic deformation causes the increase of dislocation density and the distribution of dislocations. The magnetic domain walls get pinned or held in place by dislocation interactions. Because of increased domain-wall dislocation interactions at increased plastic deformation, the magnetizing force is not high enough to set them free and reduced domain movement results in decreased BN and increased coercivity. This also results in increased hardening of the material with increased strain.

Figure (3) shows that the inverse of MBN (RMS) and H_C are linearly proportional to hardness, i.e. an increase plastic strain with a corresponding increase in hardness, results in an increase in 1/MBN and H_C.

Figures (4) and (5) show the effect of annealing on hardness, H_C and MBN. These specimens were uniformly plastically strained to 17.5% before heat treating. An examination of the plot shows that the MBN has low level between 100ºC to about 500ºC where the material is in its hardest state. This would correspond to the high dislocation density levels

within the material and associated domain-wall interactions. The slight increase in the MBN measurement at 300ºC was due to superfluous material distortion brought about during material preparation.

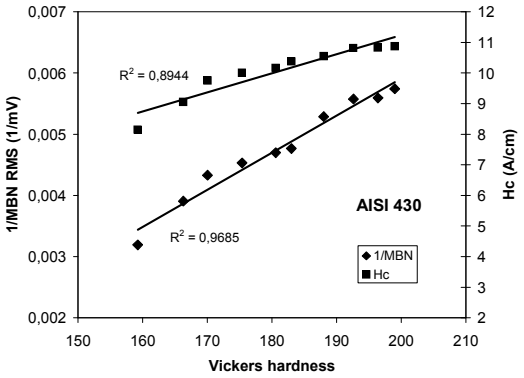

Fig. (3) Dependence of the inverse of MBN and coercivity on Vickers hardness for AISI 430

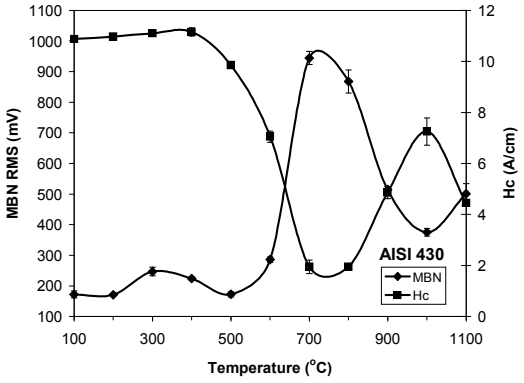

Fig. (4) MBN and HC as a function of heat treatment temperature for AISI 430

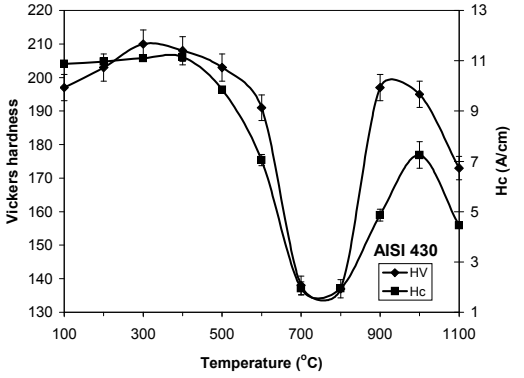

Fig. (5) Hardness and HC as a function of heat treatment temperature for AISI 430

Above 500ºC temperature, the MBN increases, H_c decreases and the annealing of the material can be seen to begin from the hardness measurements. The recovery process of the dislocations in which they begin to rearrange themselves occurs here. But it is between 700-800ºC that the material is fully annealed. In this range, the dislocation density of the specimens is relatively low and additionally large carbide grains appear within the ferromagnetic grains (Fig. 6a). These large carbides can not delay effectively the dislocation and domain wall movement as well. Thus the domain wall-dislocation interactions are at their lowest, leading to greater MBN. Therefore, this is the state where the minimum hardness and maximum ductility, toughness, and corrosion resistance of the material occurs.

The increase in hardness above 800ºC occurs because of austenite-martensite embrittlement. Because these samples were cooled in air, they become brittle due to small volumes of austenite transforming to martensite [6].

5. Conclusion

Magnetic Barkhausen noise (MBN) and conventional magnetic measurements were used to characterise the microstructural state of ferritic stainless steel. The 1/MBN and H_C values were found to be inversely proportional to hardness. In both the plastically strained and heat-treated samples, the magnetic Barkhausen noise (MBN) measurement and the magnetic parameters derived from hysteresis loop are seen to be comparable. Barkhausen noise measurement can be used as an effective means for ferritic stainless steel microstructural characterisation.

References

[1] W.S. Brandão et al., *Welding Int.*, 6 (1992) 713.

[2] V.T.L. Buono, B.M. Gonzalez and M.S. Andrade, *Scripta Materialia*, 38(2) (1998) 185-190.

[3] D.C. Jiles and D.L. Atherton, *J. Phys. D: Appl. Phys.*, 17(6) (1984) 1265-1281.

[4] M.J. Sablik, *J. Appl. Phys.*, 74 (1993) 5899.

[5] J. Dobránszky and P.J. Szabó, *Mater. Sci. Forum*, 414-415 (2003) 189-194.

[6] ASM Handbook, **"Metallography and Microstructure"**, Vol. 9 (1988).

Majed A. Al-Barzanchy
Ibrahim K. Hama
Golan M. Najeeb

Department of Physics,
Alsulaimaniyah University,
Alsulaimaniyah City,
Kurdistan Region, Iraq

Temperature-Dependent Birefringence Properties of $Be_3Al_2Si_6O_{18}$ Crystal

The temperature dependence of the refractive indices for ordinary and extraordinary rays of mercury spectrum three lines and laser line independently one from the other were measured in temperature interval 20-600℃. It was obtained that the refractive indices increase along with the temperature growth and this dependence has quasilinear character. Emerald has quite low birefringence values that increases slightly along with the temperature growth and decreases with wavelength growth. The thermooptical coefficients for every wavelength were calculated. They have greater values for the extraordinary beams than for the ordinary ones. The dispersion curve for refractive indices was obtained.

Keywords: Birefringence, Optical properties, BASO crystal, Refractive index
Received: 22 October 2008, Revised: 2 November, Accepted 9 November 2008

1. Introduction

Light is the ultimate means of sending information to and from the interior structure of materials - it packages data in a signal of zero mass and unmatched speed. However, light is, in a sense, 'one-handed' when interacting with atoms of conventional materials. This is because from the two field components of light - electric and magnetic - only the electric 'hand' efficiently probes the atoms of a material, whereas the magnetic component remains relatively unused because the interaction of atoms with the magnetic-field component of light is normally weak [1].

Metamaterials, that is, artificial materials with rationally designed properties, can allow both field components of light to be coupled to meta-atoms, enabling entirely new optical properties and exciting applications with such 'two-handed' light. Among the fascinating properties is a negative refractive index. The refractive index is one of the most fundamental characteristics of light propagation in materials. Metamaterials with negative refraction may lead to the development of a super-lens capable of imaging objects and fine structures that are much smaller than the wavelength of light.

Other exciting applications of metamaterials include antennae with superior properties, optical nanolithography and nanocircuits, and 'metacoatings' that can make objects invisible.

Emerald is a green beryl with the following chemical formula of $Be_3Al_2Si_6O_{18}$ with Cr impurity responsible for its green color. The crystal belongs to the hexagonal system and is optically positive. Si_6O_{18} rings form structure channels, which are parallel to unique axis. Octahedral positions occupied by Al in the beryl structure, may be substituted by Cr, Fe^{3+}, Fe^{2+}, Mg and Li; alcali and alcaline earth ions occupy the centers of Si_6O_{18} rings and water molecules lie centrally between the Si_6O_{18}. The limited amount of Cr is necessary for creation gem quality emerald (0.2-0.3%) [2].

The filling of the channels in the beryl structure with alcali ions and water molecules is the main cause of the variation in refractive index and density of natural beryl and emerald.

The increase of activity in the area on synthetic emerald appears to be due both to its utility as a gemstone and its reported use as a solid state maser crystal. Besides emerald can be used in low-noise microwave amplifiers as well as serve as the most effective laser medium in the range 450-600nm.

Single crystals of emerald were grown from flux melt [3] on oriented seeds in dynamical regime. Double system oxides of lead and vanadium was used as a flux. As numerous experiments on crystal growth in flux melt with correlation V_2O_5/PbO from 8/2 to 2/8 showed, it is preferably to use solvents with the equal or slightly shifted to the side V_2O_5 ratio of oxides. The cuts of single crystals, grown by the method of spontaneous crystallization, parallel to the natural prism $(10\bar{1}0)$ and $(11\bar{2}0)$ faces and pinacoid (0001) faces served as seeds. The seeds were arranged parallel each other in the planes oriented perpendicular to the flux melt surface and fixed to specially shaped platinum holders. Such configuration provides continuous washing of the growing crystal face and stirring of the melt at optimal rotation rate 30rs/min. The total area of the seed plates varied from 600mm^2 to

2000mm^2 depending on the crucible volume and the flux melt mass. The optimal experiment cycle lasted, in the average, for 3-4 months. The best single crystals grown in the experiment were almost perfect in terms of the optical parameters weighting as much as 150 carats.

2. Experimental

Refractive indices of the ordinary and extraordinary rays were measured during continuous heating or cooling of prisms cut out from crystals in such a way that the optic axis was parallel to the prism edge and the light beam propagated through the prism perpendicular to the optical axis. The size of prism was nearly 6x6x7x4mm, where 6 and 7mm was the sides of the triangular basis of prism and 4mm was its height. The least deviation method is used. He-Ne laser and a mercury lamp were sources of light. The temperature dependence of the refractive indices of mercury spectrum three lines and laser line independently one from the other was measured. The measurements were performed for the next wavelengths of mercury emission lines: violet, 4647Å; green, 5461Å; yellow, 5852Å and for laser line, 6328Å with a step 4°-5° using a GS-5 goniometer-spectrometer. The heating (cooling) rate did not exceed 0.5K/min and the sample temperature was measured with a platinum-rhodium thermocouple with an accuracy of 0.1K.

3. Results and Discussion

Temperature dependences of refractive indices for ordinary and extraordinary rays at different wavelenghts are shown in Fig. (1). It is obtained that the refractive indices increase along with the temperature growth and this dependence has quasilinear character. Emerald possesses the following refractive indices at the room temperature:

for λ=464.7nm n_e=1.5770; n_o=1.5731;
for λ=546.1nm n_e=1.5673; n_o=1.5635;
for λ=585.2nm n_e=1.565.6; n_o=1.5619;
for λ=632.8nm n_e=1.5646; n_o=1.5612,

where n_o and n_e are ordinary and extraordinary refractive indices.

Curve n1 belongs to ordinary rays of red laser line, and curve n2 belongs to extraordinary rays of red laser line; curves n3, n5 and n7 reflect the temperature dependence of refractive indices of ordinary rays for green, yellow and violet lines of mercury spectrum, and curves n4, n6 and n8 are the temperature dependence of refractive indices of extraordinary rays for green, yellow and violet lines of mercury spectrum

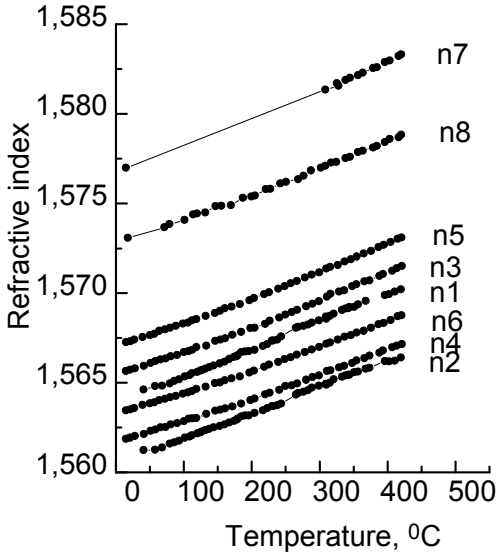

Fig. (1) Temperature dependence of refractive indices of ordinary and extraordinary rays for four different wavelengths

We should note that emerald refractive indices just slightly change along with the temperature growth. The temperature dependence curves (images of collimator slit) for all the spectral lines are practically parallel. That means that the thermooptical coefficients are almost the same for all wave lengths of both ordinary and extraordinary rays. They are slightly greater for the extraordinary rays than for the ordinary ones, 1.45-1.5x10^{-5} and 1.2-1.4x10^{-5} accordingly. Emerald has a very low birefringence value which does not change while temperature grows. Fig. (2) shows the graph of the temperature dependence of the birefringence.

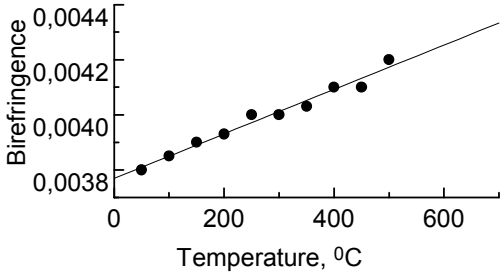

Fig. (2) Temperature dependence of birefringence (n_e-n_o) value, where n_o is refractive index of ordinary rays and n_e is refractive index of extraordinary rays

The birefringence value does not practically change while the wave length increases, i.e. the birefringence dispersion is absent. At the time the dispersion for refractive indices appears normal because refractive indices decrease along with wave length incease, Fig. (3).

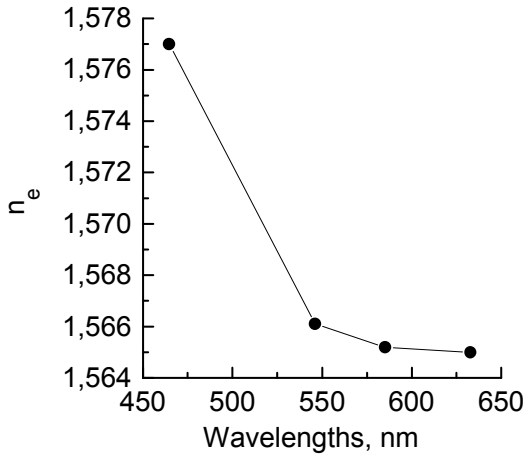

Fig. (3) Dispersion of the extraordinary rays refractive index

4. Conclusion

We should note that emerald's behaviour is quite similar to one of the inert gases or noble metalls i.e. it does not practically interact with external medium if compared to other crystals such as ferroelectrics, nonlinear crystals, semiconductors and quartz. The slight increase of refractive indices monitored while temperature increases is likely to be caused by the thermal expansion of the lattice.

The main particularity of this crystal is supposed to be the absence of any particularities in the optical properties measured by us. We can consider that absence as the main positive attraction of emerald upon its employing in dirreferent optical devices as the sinthetical emerald is much cheaper than the natural one.

References

[1] V.M. Shalaev, "Optical negative-index metamaterials", *Nature Photonics*, 1 (2007) 41-48.

[2] E.M. Flanigen et al., "Characteristic of synthetic emeralds," The American Mineralogist, Vol. 52 (May-June 1967).

[3] S.N. Barilo et al., *J. Crystal Growth*, 198/199 (1999) 716-722.

Haitham M. Mikhlif

Illumination and Dark Current-Voltage Characteristics of Polymer-Silicon Heterojunction Solar Cells

Department of Physics, College of Science, Al-Mustansiriya University, Baghdad, Iraq

In this work, polymer-on-silicon solar cells were fabricated by coating different silicon substrates with conductive polyaniline layers. Different substrates with different resistivities were used to control the diffusion length of such configurations. Electrical measurements were performed in both illumination and dark conditions to study the characteristics of photo-generated carriers in the polymer layer contributing to the output of such solar cells. They show good agreement with the "hole mobility only" model for intensities ranging from 1% of AM1.5 up to AM1.5. In addition to low-cost fabrication and less-complex technology, such design interestingly compete the conventional and advanced configurations of solar cells.

Keywords: Solar cells, Silicon devices, Conductive polymers, Amorphous silicon
Received: 9 November 2008, Revised: 31 December 2008, Accepted 7 January 2009

1. Introduction

After 20 years of work on the characterization of amorphous silicon and amorphous silicon solar cells, there has been no definitive, quantitative model for how the cells work, even under restricted conditions such as the as-deposited state [1]. The beginning of amorphous-silicon photovoltaics (PV) goes back to 1965, when Sterling et al. [2] reported deposition of silicon onto a substrate using a silane glow discharge. Hydrogenated amorphous silicon nitride layers have been intensively investigated during the last decade. The big interest in these layers is caused by their exceptional physical properties [3]. The improved set of measurements involves the use of a thickness series of cells and of a near-infrared laser to obtain uniformly absorbed illumination [4]. The solar conversion efficiency of as-deposited pin a-Si:H solar cells can be explained surprisingly well from hole mobility and optical absorption measurements on the intrinsic layer material [5].

Both solar cell materials (c-Si wafers, polycrystalline and amorphous thin films) as well as solar cells itself are investigated by photoconductivity methods in view of their recombination parameters characterisation. The efficiency of a solar cell is influenced by recombination parameters, e.g., the bulk minority carriers lifetime, the emitter saturation current and the effective surface recombination velocity [6].

Since its first successful application to amorphous semiconductors in the early 1980's [7], exponential-bandtail multiple-trapping (usually abbreviated as simply "multiple-trapping" or "MT") has become the standard approach to analyzing most transport experiments in hydrogenated amorphous silicon (a-Si:H) and related materials such as amorphous silicon-germanium alloys. The model assumes an exponential bandtail of localized states lying at the bottom of the conduction band, or at the top of the valence band. The application to transport also assumes the existence of a "transport edge," with the property that the only carriers that contribute to electrical transport are those occupying electronic states lying above this edge (for electrons) or below it (for holes); it has generally been assumed that this edge is the "mobility-edge" dividing localized and extended electronic states [8]. Perhaps 20 or more parameters are required if all possibly relevant electronic transport and trapping processes are treated, and veteran scientists might well despair of gaining insight from the daunting exercise of matching so many parameters to such simple measurements [9,10].

It is highly required to obtain a set of cell measurements using intense, near-infrared, monochromatic laser illumination that is uniformly absorbed in the cell [11]. Under white-light illumination, a good deal of the power generated by a single-junction cell is due to strongly absorbed illumination; models for such cells are quite sensitive to the absorption spectrum of the intrinsic and p-layers, but are less sensitive to transport and recombination properties of the intrinsic layer than are

measurements with uniformly absorbed illumination [12].

For thicker cells, the internal electric field no longer extends across the cell, and some holes photogenerated in the "back" of the cell (i.e., closer to the n/i interface) are lost to recombination. This "collapse" of the field [13] is just a consequence of the buildup of slowly-moving, positively charged holes near the p/i interface. We gain some confidence in this view because we find that reducing the incident flux by a couple of orders of magnitude noticeably improves the fill-factor. The qualitative explanation for this effect is that, for lower incident flux, there are fewer drifting holes, and less positive space-charge to collapse the voltage. The simulations agree fairly well with the measurements for fluxes in the range 10^{15}-10^{17} photon/cm^2 [14].

The open-circuit voltage (V_{OC}) is nearly independent of thickness and this essential result also emerges from the bandtail-only simulations, although there are some subtle differences in the behaviors. The hole drift mobilities and valence bandtails are the main elements determining the solar conversion efficiency of a-Si:H based solar cells in their a-deposited state. It is also plain that the conversion efficiency in the light-soaked state is markedly reduced from the as-deposited state [15].

There have been several reports of drift-mobility measurements in microcrystalline silicon in the last decade or so since it became clear that this material could be prepared with properties that are interesting for solar cells [4-8,16]. There is, of course, an enormous range of possible structures in microcrystalline silicon materials. For each sample there is a spectrum of sizes for the component nano- and micro-crystallites. Even more poorly understood, for each sample there is also a jumble of non-crystalline material that lies between the crystallites [17].

It is worth noting that disorder affects holes and electrons very differently. The conduction bandtail in amorphous silicon has a width around 22meV [18]. Electron properties in samples similar to those used in this work have been studied using post-transit time-of-flight [19]; bandtail multiple-trapping did not apply for these transients.

2. Experiment

Simple solar cells were fabricated by coating a layer of conductive polyaniline onto a silicon substrate. Two kinds of silicon substrates were used in this experiment: (i) n-type, orientation (100), R=2Ω.cm and (ii) n-type, orientation (111), R>3000Ω.cm. Large area, 50nm thick aluminum contact was evaporated onto the back (unpolished) side of the wafer. Immediately before the polymer film was applied, the silicon wafers were etched in a 2.5% HF solution. The solvent is dichloroacetic acid (DCA); the dopant is 2-acrylamido-2-methyl-1-propanesulphonic acid (AMPSA). The polyaniline solution was made following the procedure of Adams et al. [20]. The area of spin-cast doped polyaniline film was around 0.5cm^2. The films were annealed in air at 80°C for 6 hours after casting. A circular nickel contact (50nm thick) was then evaporated onto the polyaniline film. The polyaniline films were typically 5μm thick and the resistivity of the doped films was about 0.1Ω.cm.

The current-voltage characteristics were measured at room temperature with a Keithley 616 meter. The intensity-dependent measurements were done using illumination from a 632.8nm laser. The transient photocurrents were measured in the pin diodes following illumination by 532nm laser pulses (SHG Nd:YAG) through the n-layer. The photo-charge was independent of the applied voltage, and a transit-time was discernible in the transient. Additionally, the photocurrent at short times was linear in the applied voltage, which is consistent with transport that is linear with electric field.

Measurements were recorded over a wide range of illumination intensities. The more definitive set of measurements shows good agreement with the "hole mobility only" model for intensities ranging from 1% of AM1.5 up to AM1.5.

3. Results and Discussion

Figure (1) shows two current-voltage (I-V) curves for two different diodes from the same batch, using the 2Ω.cm substrate. The current-voltage (I-V) characteristics are highly asymmetrical as expected for a p-n heterostructure device; the reproducibility is fairly good. Figure (2) illustrates the I-V curves observed in one diode at several times up to about 2 weeks after its fabrication; the diode was stored in a desiccators when not under study. Interestingly, the diode's forward bias current first increases, and then recovers to nearly the initial state. As the origin of these effects; both room-temperature curing of the polymer and also room-temperature changes at the polymer-Si interface may be envisioned. Aging effects have been noted for polyaniline/c-Si diodes in previous work [21,22].

Figure (3) illustrates the effect of changing the c-Si substrate doping level. It was presumed that the higher resistance of the 3000Ω.cm substrate affected the diode principally via the

series resistance of the substrate; obviously, this effect is modest.

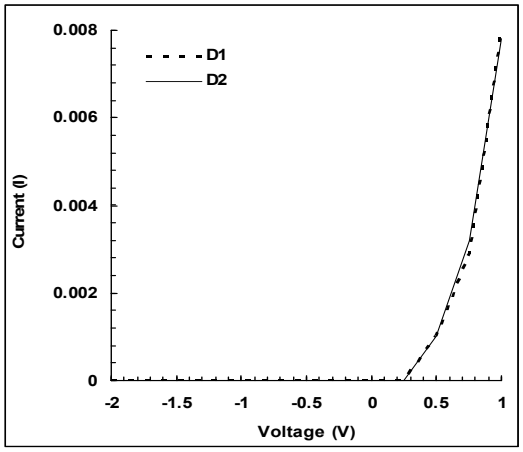

Fig. (1) Current-voltage (I-V) characteristics for two diodes from the same batch

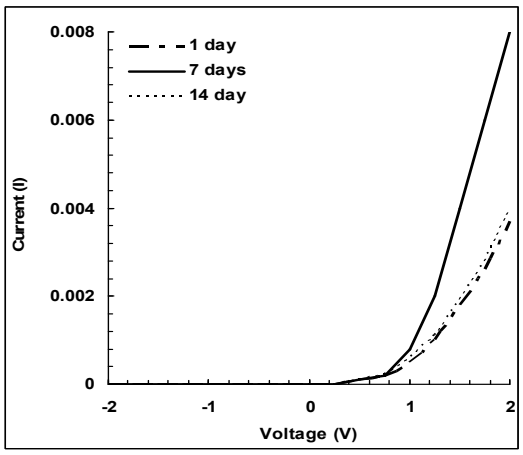

Fig. (2) Current-voltage (I-V) characteristics for c-Si/polyaniline diodes repeated at three intervals following fabrication

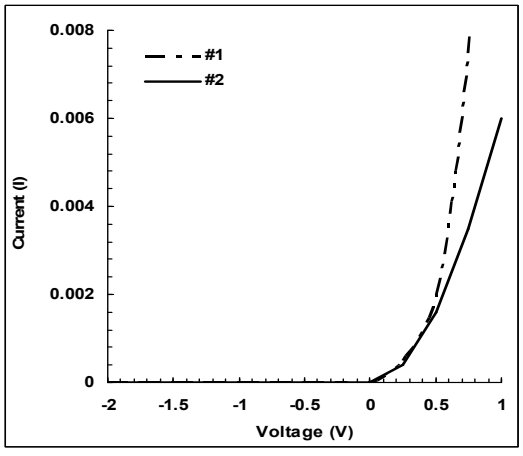

Fig. (3) Current-voltage (I-V) characteristics to c-Si/polyanile diodes with different c-Si substrates (#1, 2Ω.cm and #2, 3kΩ.cm)

The standard diode equation was fitted to these I-V characteristics. If the following standard diode characteristic equation is applied:

$$I = I_0 \exp\left[\frac{q}{nKT}\left(V - IR_S\right)\right] \quad (1)$$

where q is the electronic charge, n is the ideality factor, and R_S is the series resistance, then a straight line by a graph of I(dV/dI) vs. I is obtained from:

$$I\frac{dV}{dI} = \frac{nKT}{q} + IR_S \quad (2)$$

The fit to this form for the 2Ω.cm substrate for lower currents (<10mA) yielded n=1.8, R=49Ω; the fit for the 3000Ω.cm yielded n=1.8, R=77Ω.

Two diodes were prepared with varying polyaniline thickness on the 2Ω.cm substrate and the results are illustrated in Fig. (4). The illuminator was a 250W ENH tungsten-halogen bulb and the diode was illuminated through the polyaniline. The dark currents are fairly similar; there is slightly less dark current for the thicker diode. Under illumination, both diodes show a saturated reverse-bias current. It is surprised that the diode with the thicker polyaniline film has a larger saturation current.

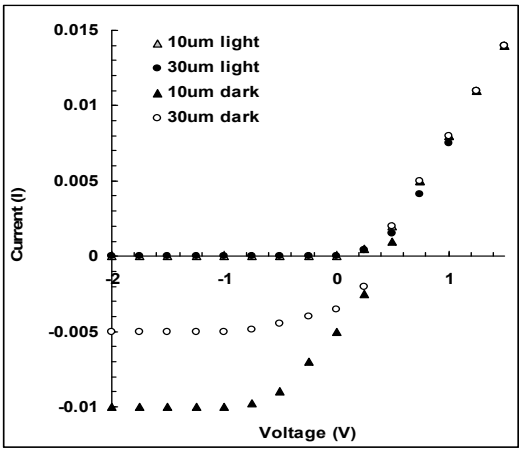

Fig. (4) dark and light I-V characteristics of two diodes with different thickness of polyaniline (10μm, 30μm) made from the same solution

Although a serious analysis of these diode properties was not conducted, it should be presumed that photo-carriers generated throughout most of the polyaniline should not contribute to the saturation current, and indeed the thicker film might have optically filtered some of the photons. It may be that the polyaniline film has different properties for the two thicknesses, at least near the c-Si interface.

Two diodes were made from two different silicon substrates. The polyaniline thickness of both diodes was 5μm. The current-voltage (I-V) characteristics of the two diodes under illumination are shown is Fig. (5) and they are quite different. Under forward bias, the principal effect appears to be that the high resistivity substrate led to a significant series resistance.

Interestingly, under reverse bias the high resistivity substrate shows a substantially larger reverse bias current. This presumably corresponds to an increased diffusion length in the higher resistivity substrate.

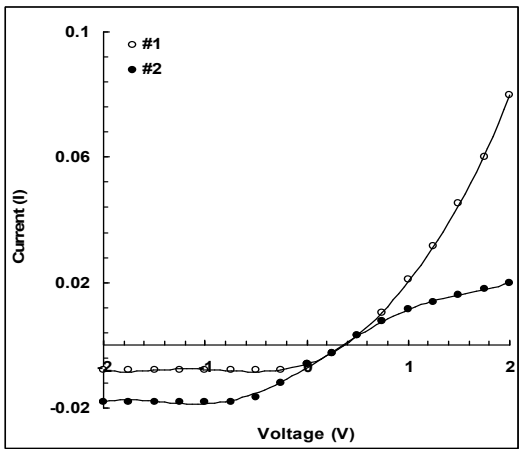

Fig. (5) Light I-V characteristics of two polyaniline/c-Si heterostructure diodes made on c-Si substrates with 2 different (n-type) resistivities (#1, 2Ω.cm and #2, 3kΩ.cm). The doped polyaniline layers were about 5μm thick

4. Conclusion

Current-voltage characteristics of polymer-silicon p-n heterojunction solar cells showed that such low cost and simple design devices show good agreement with the "hole mobility only" model for low intensities up to AM1.5 condition. The ideality factor of the prepared samples was ranging over accepted values at low illumination condition. Results explained that the substrate resistivity highly affects the electrical characteristics of such heterojunctions. Under reverse bias, the high resistivity substrate shows a substantially larger reverse bias current.

Acknowledgement

Author would like to thank Dr. Raid A.W. Ismail and Mr. Oday A. Hamadi for their valuable notes and comments as well as school of applied science at the University of Technology (Baghdad, Iraq) for experimental assistance.

References

[1] E.A. Schiff, *Solar Ener. Mater. Solar Cells*, 78 (2003) 567-595.
[2] H.F. Sterling and R.C.G. Swann, *Solid-State Electron.*, 8 (1965) 653.
[3] M. Lipiński et al., *Opto-Electron. Rev.*, 12(1) (2004) 41-44.
[4] Q. Gu, E.A. Schiff, J.-B. Chevrier and B. Equer, *Phys. Rev. B*, 52 (1995) 5695.
[5] J. Pearce et al., *Appl. Phys. Lett.*, 77 (2000) 19.
[6] T. Pisarkiewicz, *Opto-Electron. Rev.*, 12(1) (2004) 33–40.
[7] T. Tiedje, *Appl. Phys. Lett.*, 40 (1982) 627.
[8] Q. Wang, R.S. Crandall and E.A. Schiff, in Conference Record of the 21st Photovoltaics Specialists Conference (IEEE, 1996), 1113.
[9] G. Juška et al., *J. Appl. Phys.*, 89 (2001) 4971.
[10] M. Serin, N. Harder and R. Carius, *J. Mater. Sci.: Materials in Electronics*, 14 (2003) 733.
[11] J. Meier, R. Flückiger, H. Keppner and A. Shah, *Appl. Phys. Lett.*, 65 (1994) 860.
[12] O. Vetterl et al., *Mater. Res. Soc. Symp. Proc.*, 664 (2001) A25.8.
[13] T. Weis et al., *J. Appl. Phys.*, 92 (2002) 1411.
[14] L. Houben et al., *Phil. Mag. A*, 77 (1998) 1447.
[15] L.C. Chen, L.A. Hamel and A. Yelon, *J. Non-Cryst. Solids*, 220 (1997) 254.
[16] Q. Gu et al., *J. Appl. Phys.*, 76 (1994) 2310-2315.
[17] Q. Wang, H. Antoniadis, E.A. Schiff and S. Guha, *Phys. Rev. B*, 47 (1993) 9435.
[18] J.M.G. Laranjeira et al., *Appl. Surf. Sci.*, 190 (2002) 390-394.
[19] R. Atta-Fynn et al., *Phys. Rev. B*, 69 (2004) 085207.
[20] P.N. Adams et al., *J. Phys.: Cond. Matter*, 10 (1998) 8293-8303.
[21] A. Yelon, B. Movaghar and H.M. Branz, *Phys. Rev. B*, 46 (1992) 12244.
[22] A. Yelon and B. Movaghar, *Phys. Rev. B*, 65 (2002) 077202.

Employing Inner Triplet Upgrade in Cold Mass Cooling Design for Large Hadron Collider

Fahd M. Al-Shimmary
Abdul-Aziz F. Al-Maliky
Sinan H. Al-Hadithi

Department of Mechanical Engineering,
Faculty of Engineering Sciences,
King Fahd University,
Dahran, KSA

A luminosity upgrade of the CERN Large Hadron Collider (LHC) is planned to coincide with the expected end of life of the existing inner triplet quadrupole magnets. The upgraded inner triplet will have much larger heat loads to be removed from the magnets by the cryogenics system. As part of the LHC Accelerator Research Program (LARP), a design study has been completed to investigate the required characteristics of the cold mass cooling system within the framework of a design temperature profile. These characteristics are the beam pipe annulus, collar radial cooling channels, yoke radial cooling channels, yoke longitudinal cooling channels, and heat exchanger connecting pipe. Using these parameters in conjunction with energy deposition calculations, longitudinal and radial temperature profiles for an entire inner triplet are calculated and presented.

***Keywords**:* Accelerator magnets, Cooling, Cryogenics, Helium
Received: 9 November 2008, Revised: 22 December, Accepted 29 December

1. Introduction

The inner triplets of the CERN Large Hadron Collider (LHC) are expected to reach their end of life after several years of operation due to radiation damage. Subsequent replacement of the inner triplets it expected to coincide with a luminosity upgrade of the accelerator. Such an upgrade would result in increased heat loads to the inner triplet magnets, requiring a new design instead of simply replacing them with another identical triplet. A number of possible upgrade scenarios are being considered: Nb_3Sn coil magnets [1], NbTi coil magnets [2], and 'slim' quadrupole magnets placed very close to the interaction point (IP).

Cold mass cooling studies are required to ensure the heat load deposited by the beams can be removed from the cold mass within acceptable temperature limits. Inadequate cooling of the magnet coil would result in quenching when operating at high luminosity. One such cold mass cooling study is presented here for a luminosity of $10^{35}/cm^2$-s, a factor of 10 higher than the nominal luminosity of the LHC. This paper details the cooling study of an inner triplet consisting for four main quadrupoles and four correctors. The four main quadrupoles are Q1 (closest to the IP), Q2a, Q2b, and Q3 (farthest from the IP). The four corrector magnets are MCBX-1 (a nested horizontal and vertical dipole orbit corrector at the non-IP end of Q1), MCBX-2 (a nested horizontal and vertical dipole orbit corrector between Q2a and Q2b), MQSXA (a skew quadrupole in line with nested skew octupole, octupole, and skew sextupole coils at the Q3 IP end), and MCBXA (an MCBX package with nested sextupole and dodecapole coils at the Q3 non-IP end). This inner triplet would be placed on either side of the IP at the position of the existing inner triplet. The cold mass magnetic lengths are 6.3 m for Q1 and Q3, and 5.5m for Q2a and Q2b. The coil aperture is 90mm. The beam pipe is made of the tungsten-rhenium alloy W-25 Re with a thickness of 11.5mm in the Q1 and 2.5mm elsewhere. The inner triplet operates in a stagnant bath of He II that is cooled by a He II heat exchanger located outside the cold mass. The external heat exchanger currently used in the inner triplet is described elsewhere [3,4], as are initial heat exchanger studies for the upgraded inner triplet [5].

This paper presents the methodology used to calculate the values for the critical cooling parameters for this particular configuration. Radial and longitudinal temperature profiles are then calculated for single magnets and the entire inner triplet from the beam pipe annulus to the magnet heat exchanger.

2. Design and Magnet Temperature Profile

A design temperature profile was established as a starting point for the cold mass cooling studies. The design temperature profile takes the total temperature drop in the cryogenic system, from the magnet beam pipe to the cryoplant cold

compressors, and partitions it into segments with the ultimate goal of ensuring the magnet coil remains in He II.

There were several considerations in arriving at the design temperature profile. An initial study examined the thermal limitations of the existing inner triplet and identified thermal bottlenecks as the heat load is increased [6]. These bottlenecks were then allocated a relatively larger temperature drop.

Another consideration is possible upgrades to the LHC cryogenics system. For example, upgrading the cold compressors and moving them closer to the inner triplets would increase the available temperature drop and reduce the pressure drop in the piping between the inner triplets and cold compressors.

Finally, CERN work in the Next European Dipole (NED) program and interaction region upgrade studies also provided input for the design temperature profile [7,8].

The design temperature profile used for this design study allocates a 150mK temperature drop (2.15-2.00K) from the beam pipe annulus to the heat exchanger connecting pipe, and a 50mK temperature drop (2.00-1.95K) within the heat exchanger connecting pipe. The envisioned heat exchanger connecting pipes are illustrated in Fig. (1).

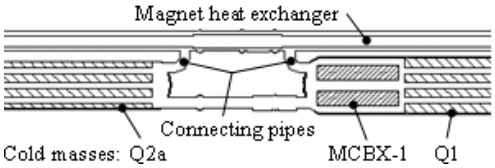

Fig. (1) Illustration of heat exchanger connecting pipes, which transfer heat from the cold mass He II volume to an annular He II volume around the heat exchanger pipe. Results presented here assume a connecting pipe at each end of each cold mass, as shown

The existing inner triplet has one connecting pipe per interconnect, whereas it is assumed the upgraded inner triplet will have a connecting pipe at each end of each main cold mass.

A required input to calculate temperature profiles is the longitudinal heat deposition. Figure (2) shows the calculated dynamic heat load to the He II as a function of distance from the IP [9]. The locations of the four main quadrupole cold masses are indicated. The four corrector magnets are also shown, each indicated by a single vertical bar outside the brackets of the main quadrupoles. The heat is assumed to be deposited equally in the horizontal and vertical planes. Radial variations in heat deposition are also not taken into account. Whether heat is deposited in the beam pipe, the inner coil, or the outer coil, it is assumed that all heat reaches the He II of the beam pipe annulus.

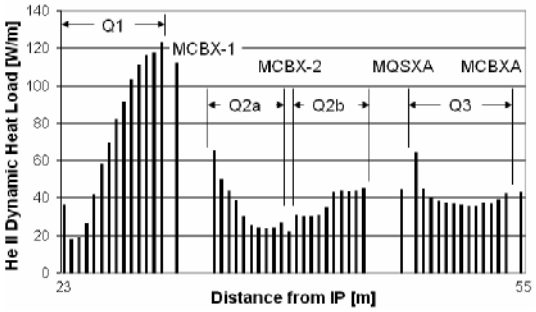

Fig. (2) Dynamic heat loads to the He II system of the upgraded inner triplet. Increasing the LHC luminosity would substantially increase the He II heat loads, requiring careful design of the cold mass cooling system

The thermal center is the longitudinal position where there is a change in the direction of heat flow. On the IP side of the thermal center, heat flows toward the IP. On the non-IP side of the thermal center, heat flows away from the IP. The thermal center provides a zero heat flux boundary condition for subsequent calculations.

A first estimate of the longitudinal position of the thermal center of a cold mass is calculated by (1), where $q(x)$ is the heat flow at a given position, L is the length of the cold mass, and x_{TC} is the longitudinal position of the thermal center. The cubic exponent is characteristic of He II heat transfer. Equation (1) assumes the longitudinal temperature drops from the thermal center to each end of the cold mass are equal.

$$\int_0^{x_{TC}} q^3(x)\,dx = \int_{x_{TC}}^{L} q^3(x)\,dx \qquad (1)$$

Based on the calculated location of the thermal center of each main quadrupole cold mass, Figure (3) shows the amount of heat to be removed from each end of each cold mass. The numbers in parentheses are the heat loads deposited in the corrector magnets. The numbers without parentheses are the heat loads deposited in the main quadrupoles.

There are a number of critical design features that must be specified in order to adequately remove heat from the cold mass coils: beam pipe annulus, collar radial cooling channels, yoke radial cooling channels, yoke longitudinal cooling channels, and heat exchanger connecting pipe. The sensitivity and effect of each individual parameter can be studied using (2), where q'' is the heat flux, L is the cooling channel length, $f^{-1}(T,P)$ is the He II thermal conductivity function, and T is temperature.

$$q'' = \left(\frac{1}{L} \int_{T_1}^{T_2} f^{-1}(T,P)\,dT \right)^{1/3} \qquad (2)$$

Heat exchanger connecting pipes transfer heat from the ends of the cold masses to the

external heat exchanger. Each inner triplet now has five connecting pipes: one at the IP end of Q1, one between each pair of cold masses, and one at the non-IP end of Q3. Those at the Q1 IP end and at the Q3 non-IP end have an inner diameter of 82.8mm. Those in the interconnects have an inner diameter of 95.2mm. The maximum size of this connecting pipe is limited by the geometries of the cold mass and cryostat piping. The cooling scheme presented here uses pipes having a 168.3mm (6.625in) outer diameter and a 3.4mm (0.134in) wall thickness.

For the Nb_3Sn magnets being studied here, [1] has specified 400cm^2 of yoke longitudinal cooling channels. The existing inner triplet magnets have 113cm^2.

Yoke radial cooling channels are required to transfer heat from the yoke lamination inner diameter to the yoke longitudinal cooling holes. These cooling channels may be created by removing a small portion of the full thickness of the yoke lamination at the parting plane or by machining cooling channels into the surface of the laminations. Whichever method is used, it must be ensured that the heat load is able to be distributed among the yoke longitudinal cooling holes. The cooling scheme described here considers 2.4% of the yoke inner diameter open for cooling channels.

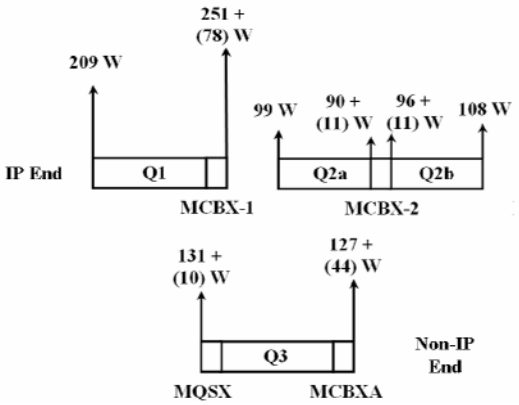

Fig. (3) Heat loads to be removed from each end of each inner triplet quadrupole. These values result from estimating the locations of the cold mass thermal centers using (1)

Collar radial cooling channels are required to transfer heat from the beam pipe annulus to the iron yoke. Collar cooling channel size is expressed as a percentage of the collar pole tip open for He II heat transfer. The current LHC Q2 quadrupole magnets have a cooling channel equivalent to 4% of the inner pole tip area, or one missing 1.5mm thick collar lamination in each quadrant per 38mm of length. If the second generation magnets are constructed similarly to the first generation magnets, it is recommended to have a collar cooling channel area equivalent to 7% of the pole tip area, or one missing 1.5mm thick lamination in each quadrant per 21mm of length.

A heat load due to secondary particles produced by the proton-proton collisions at each IP is deposited in the beam pipe and the coils, concentrated in the horizontal and vertical planes. This heat is transferred to the He II and is conducted 45^o circumferentially through the beam pipe annulus to the collar pole tips. The existing inner triplet has a 1mm annular gap between the beam pipe and the coils. The same 1mm annular gap is used here.

This is one possible combination of parameters and is summarized in Table (1). The value of each parameter is noted along with the calculated radial temperature drop near the non-IP end of Q1, where the heat loads are largest. The maximum calculated temperature is 2.089K, leaving a significant temperature drop available from the coil to the He II bath.

Table (1) Cold mass cooling system parameters

Design parameter	Value	Calculated temperature range [K]
Beam pipe annular gap	1 mm	2.089 - 2.061
Collar radial cooling channels	7% of collar pole tip open	2.061 - 2.008
Yoke radial cooling channels	2.4% of yoke inner diameter open	2.008 – 2.000
Yoke longitudinal cooling channels	400 cm^2	2.000
Heat exchanger connecting pipe	161.5 mm (6.357 in) inner diameter	2.000 - 1.971

3. Results and Discussion

Once these parameters have been specified, the longitudinal and radial temperature distribution of one half of the cold mass (from the thermal center to the cold mass end) can be calculated. A finite difference model using temperature-dependent properties of He II was constructed to calculate the temperature profiles. Figure (4) shows the resulting temperature map of the non-IP half of Q1 where the heat loads are the highest, resulting in substantial temperature gradients.

It was assumed that all heat transfer is radial, except in the yoke longitudinal cooling holes. The beam pipe annulus allows a slight redistribution of the heat load, permitting it to find a path of least resistance through the cold mass cooling channels. The result would be a slight smoothing of the calculated magnet temperature profiles. Neglecting this effect is therefore conservative in that a larger temperature range is calculated. This redistribution of the heat load has been calculated to be 3W/m or less, which is small compared to the dynamic heat loads presented in Fig. (2).

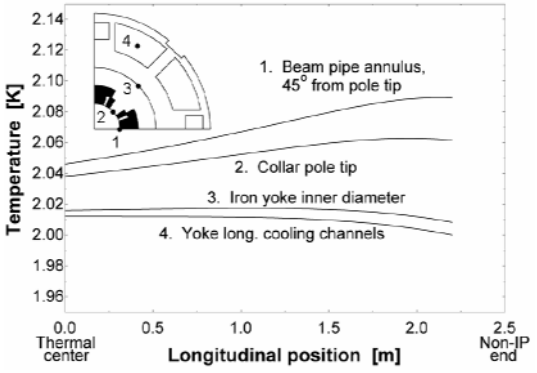

Fig. (4) Temperature profile of the non-IP half of Q1. All locations within the magnet remain in He II, below the lambda point of 2.17K. The yoke longitudinal cooling channels are 2.00K at the non-IP end of the cold mass as specified by the design temperature profile. At the thermal center, the temperature gradient in the yoke longitudinal cooling channels is zero

These calculations can be extended to calculate the radial and longitudinal temperature profiles of the entire inner triplet. The finite difference model was applied to each half of each cold mass to calculate the temperature profiles after additional iterations to more precisely locate the cold mass thermal centers and generate better curve fits of the longitudinal heat load distribution. This and the temperature-dependent properties of He II account for the difference at the non-IP end of Q1 between Fig. (4) and Fig. (5), which presents the calculated temperature profile of the specific inner triplet configuration considered here. Discontinuities in the temperature curves are the result of small errors in determining the exact thermal centers of the magnets.

8. Conclusion

A methodology for calculating longitudinal and radial temperature profiles of an inner triplet has been presented. A complete thermal analysis also requires consideration of the heat exchanger and heat transfer between the coil and the He II. While results for one specific inner triplet configuration and cold mass geometry are detailed here, this approach can be used to investigate other inner triplet configurations. One such alternate configuration is the use of heat exchanger tubes internal to the cold mass [10]. Convergence on a magnet design will ultimately require iteration on both thermal and mechanical analyses.

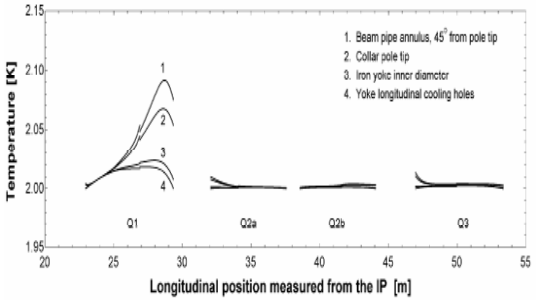

Fig. (5) Calculated longitudinal and radial temperature profiles of the inner triplet. The cooling system presented here would result in sizable temperature drops in the Q1 cold mass but very small temperature drops in the other cold masses. The positions where temperatures are calculated are the same as those identified in the Fig. (4) inset

References

[1] A.V. Zlobin *et al.*, *IEEE Trans. Applied Superconductivity,* 13 (2003) 1266-1269.

[2] O. Brüning, R. De Maria, R. Ostojic, "Low Gradient, Large Aperture IR Upgrade Options for the LHC compatible with Nb-Ti Magnet Technology," CERN LHC Project Report 1008 (May 2007).

[3] P. Lebrun, L. Serio, L. Tavian, and R. Van Weelderen, *Adv. in Cryogenic Engineering*, 43A (1998) 419-426.

[4] R. Byrns *et al.*, *Proc. of the 17th Int. Cryogenic Eng. Conf. 14-17 July 1998*, 743-746.

[5] R. Rabehl and Y. Huang, *Adv. in Cryogenic Eng., Trans. of the Cryogenic Eng. Conf.* - CEC, 53 (2008), 333-340.

[6] R. Rabehl, "LARP IR Cryogenics: Scaling of LHC I IR Cryogenics Model," Document LARP-doc-15.

[7] R. van Weelderen, "He II Heat Transfer in Superconducting Magnets," Next European Dipole (NED) project, February 2005.

[8] R. van Weelderen, "Heat Transfer in Superconducting Magnets," Accelerator Magnet Technology (AMT) – Beam Generated Heat Deposition and Quench Levels for LHC Magnets, March 2005.

[9] N. Mokhov and I. Rakhno, Fermi National Accelerator Laboratory, Batavia, IL, private communication, January 2006.

[10] R. Rabehl, "LARP IR Cryogenics: Inner Triplet Heat Transfer Studies," Document LARP-doc-364.

Selma M.H. Al-Jawad

School of Applied Sciences,
University of Technology,
Baghdad, Iraq

Effect of pH Value on the Photoconductivity of Chemically Deposited CdS Thin Films

Highly photosensitive CdS thin films with photocurrent to dark current ratio (I_{ph}/I_d) of ~10^5 under 300W.m^{-2} illumination were reported. The films are prepared by an electroless chemical deposition technique. The pH value of the solution used in the electroless deposition of cadmium sulfide thin films has been found to affect the deposition rate, optical transmission, photoconductivity, photoconductivity to dark conductivity ratio σ_{ph}/σ_d and photocurrent decay time.

Keywords: CBD, Polycrystalline CdS films, Optoelectronic characteristics
Received: 20 July 2008, Revised 31 October 2008, Accepted: 7 November 2008

1. Introduction

Current interest in direct energy conversion devices has led to renewed research in the area of materials for such devices [1-3]. Cadmium sulfide thin films can be prepared by different methods such as vapor deposition, sputtering, chemical spray deposition and chemical bath deposition. CdS has been widely accepted as one of the most sensitive photoconductors and its status as promising thin film solar cells material is sustaining continued interest in this material [4]. In the context of the need for a simple yet reliable technique for producing large area cells of CdS of high stoichiometry, this report on the preparation of chemically bath deposited films would appear to be topical. Various factors affecting the deposition process have been studied in order to understand the process of deposition and thus to improve the characteristics of the films.

The basic mechanism of the film formation in this technique is an ion-by-ion condensation of Cd^{2+} and S^{2-} ions on the substrate from an aqueous basic medium, pH>10, containing thiourea and cadmium ions. The cadmium ions are present in the form of a complex species in solution, the dissociation of which causes the slow release of Cd^{2+} ions for the formation of the thin film [4]. In the case where thiourea is employed in an alkaline medium, the sulfide ions are released as follows [5]:

$$Sc(NH_2)_2 + OH^- = CH_2N_2 + H_2O + SH^- \quad (1)$$

$$SH^- + OH^- = S^{2-} + H_2O \quad (2)$$

Using $CdSO_4$ with ammonia (NH_4OH) will form cadmium complex $[Cd(NH_3)_4]^{2+}$ according to the following equation [6]:

$$CdSO_4 + 2NH_3 = [Cd(NH_3)_4]SO_4 \quad (3)$$

Then CdS will form according to the following equation:

$$[Cd(NH_3)_4]_{2+} + S^{2-} = CdS + 4NH_3\uparrow \quad (4)$$

Our major interest in this work was the development of CdS thin films of high photoconductivity to serve as window material in heterojunction solar cells [7,8].

2. Experiment

2.1 Chemical deposition of the films

Substrates of borosilicate glass slides were used for deposition. They were first cleaned in distilled water in order to remove the impurities and residuals from their surfaces then rinsed in chromic acid for 24 hours to introduce functional groups called nucleation and/or epitaxial centers, which form the basis of the thin films growth [9]. Then the samples were washed repeatedly in deionized water and finally put in ultrasonic agitation with distilled water for 15min then dried.

The deposition of CdS films is achieved from dilute solutions. Sulfide ions are released in the bath by the hydrolysis of thiourea, in the presence of OH^- ions. Cd^{2+} ions are complexed with one or more of the complex agents like NH_3 [directly added as NH_3(aq)], or NH_4Cl. This ensures slow release of Cd^{2+} ions in the solution [10]. Films were deposited on glass slides using slowly-mixed 0.1M ($3CdSO_4.8H_2O$), NH_3 solved in distilled water at room temperature with continuous stirring. Substrates were then immersed in a beaker containing the reaction mixture. The beaker was placed in a water bath at temperature of (80±2°C). It was heated with continuous stirring to the required temperature of deposition. The solution was stirred with a magnetic stirrer type (MSH-300). Then 30ml of

0.2M thiourea solution was added with continuous stirring. The pH was measured with pH-meter type (BIBBY 211). After 20 minutes, substrates were then taken out and washed with distilled water and ultrasonic agitation to remove the porous cadmium sulfide over layer, then dried.

2.2 Measurements

In order to measure the electrical properties of 2cm^2 samples, ohmic contacts were made by vacuum evaporation of high-purity (99.999) indium wire. Evaporation process was started at a pressure of 10^{-5}torr and the best condition for good ohmic contact was satisfied by a layer of 200nm, which was determined by weighing method.

In illumination measurements, a halogen lamp connected to a variac and calibrated by power meter, was used. The bias and current measurements were performed using Keithley-602 electrometer and d.c. voltage source. The bias was 10V in all cases. The photocurrent response was measured for total duration of 1600s for each sample as follows: the first 200s in dark, the subsequent 400s under 300W.m^{-2} simulated solar radiation and the last 1000s with the illumination shutoff to facilitate the dark decay of the photocurrent. All measurements were done at room temperature (24°C).

A Cecile CE-7200 spectrophotometer supplied by Aquarius company was used to introduce the optical transmission for CdS thin films deposited on glass substrates in the wavelengths range (375-900) nm.

3. Results and Discussion

3.1 The optical transmission

The spectra shown in Fig. (1) represent the transmittance of the films deposited at different pH values. It was found that the transmittance of the deposited films is high at long wavelengths (70-80%) and decreases to 10% at short wavelengths. This is mainly because of the increased abundance and/or size of the single crystallite overgrowth. The increase and decrease in the transmittance during the continuous increase of [pH] is attributed to the transition of CdS phase from mixed cubic and hexagonal to hexagonal structure. With this result, pH of 11.5 is thought to be the optimum value to deposit CdS films used for photovoltaic applications.

3.2. The dark conductivity

The photocurrent response of the films deposited at different pH values are shown in Fig. (2). Some small random variation in the dark current level was observed. However, the stable dark current levels in all cases in Fig. (2) were found at about 10^{-11}A at 10V bias. The variations in deposition time do not cause any significant change in the conductivity and this emphasizes the preference for stoichiometry of the chemically deposited CdS thin films. This aspect was earlier studied by Danaher et al. [11], whose x-ray photoelectron spectroscopy studies yielded a normalized Cd:S ratio of 1.04±0.08 in the chemically deposited CdS films.

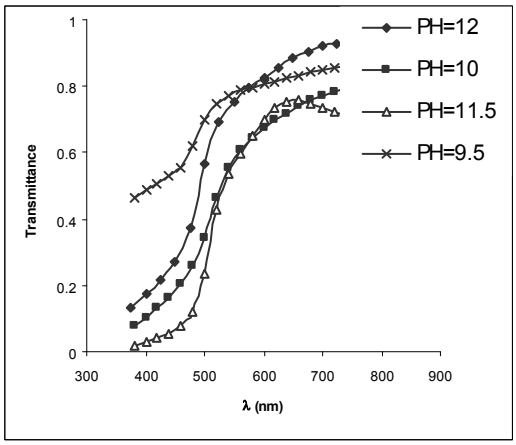

Fig. (1) The optical transmission spectra of CdS films for different pH value

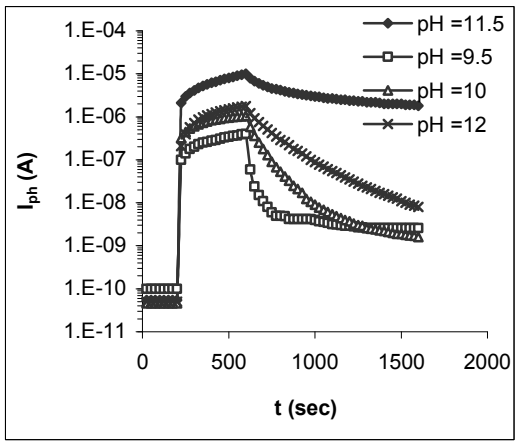

Fig. (2) Photocurrent response of the CdS films deposited for different pH value

3.3 The photoconductivity

The effect pH value on the photoconductivity of the chemically deposited CdS thin films are very significant, as seen in Fig. (2). The variation in the photoconductivity with pH values is explicitly shown in Fig. (3).

It is generally accepted that the photoconductivity in CdS thin films follows the models of Orton et al. [12]. On the basis of these models, the photoconduction in CdS films is mainly ascribed to photogenerated electrons. The photogenerated holes make a rather indirect contribution by enhancing the electron mobility when the trapping of photogenerated holes at the inter-grain barriers reduces the barrier height, thereby promoting the electron transport [14].

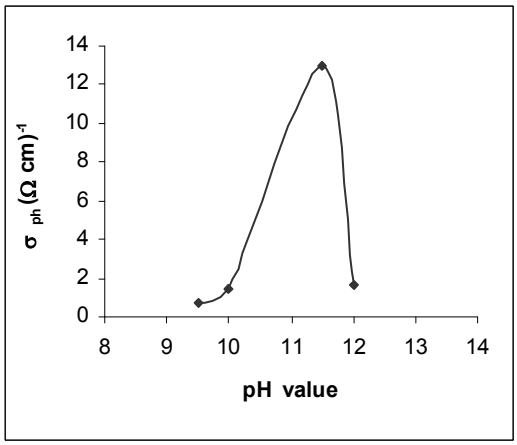

Fig. (3) Photoconductivity of the CdS films recorded at the end of 10 min of illumination (300 W m^{-2} simulated solar radiation) for different pH value

The variation in the photoconductivity in different films under the same illumination condition, as in the present work, can arise from the variation in either the electron mobility (μ_n) or the free lifetime (τ_n) of the photogenerated electrons in the equation [13]

$$\sigma_{ph} = eG\mu_n\tau_n \quad (5)$$

where σ_{ph} is the photoconductivity, e is the electron charge and G is the photo-carrier generation rate, which in the present case (300W.m^{-2}) is estimated to be about 10^{20} electron-hole pairs.cm^{-3}.s^{-1}. The maximum photoconductivity of 1.32(Ω.cm)$^{-1}$ (at 90^{o}C) observed in this work yields the mobility-lifetime product for electrons as $\mu_n\tau_n$~0.1cm^{-1}V^{-1}.

Since the measurement of the mobility was not performed, it was not possible to ascertain if the increase in the mobility-lifetime product with the decreasing bath temperature is due to the increase in mobility or due to an increase in the carrier lifetime. In polycrystalline CdS films, there is an increase in electron mobility due to increase in grain size [14]. The higher mobility-lifetime product increases the diffusion length (L) and leads to an increased short-circuit current. Also, since the series resistance of the cell is inversely proportional to the carrier mobility, as well as to the carrier concentration, higher carrier mobilities are desirable in such applications. The variations in mobility-lifetime with pH values are shown in Fig. (4).

3.4 The photocurrent decay time

Figure (5) shows the variations in the photocurrent decay time with pH value. The decay time refers to the time required for the photocurrent value attained at the end of exposure (400S, 300W.m^{-2} illumination) to decay to 1/e of this value.

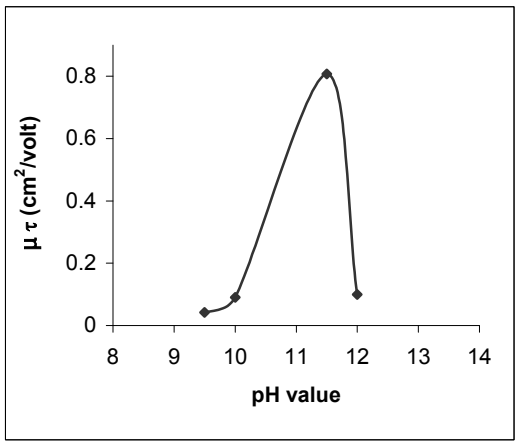

Fig. (4) The variation in mobility-lifetime with pH value

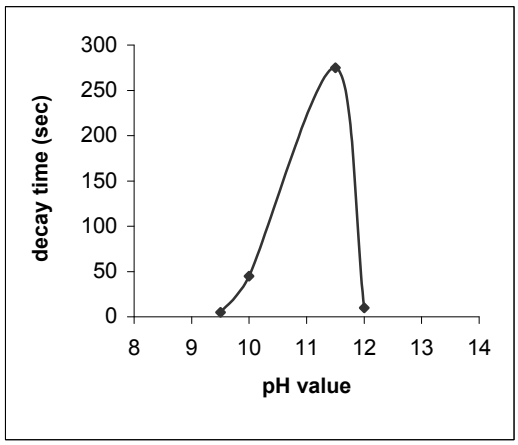

Fig. (5) Effect of the pH value on the photocurrent (300W.m^{-2} simulated solar illumination) decay time

3.5 The photocurrent-to-dark current ratio

Figure (6) shows the photoconductivity-to-dark conductivity ratio (σ_{ph}/σ_d) for the deposited films as a function of pH value. Values of the above ratio are among the highest reported for CdS films.

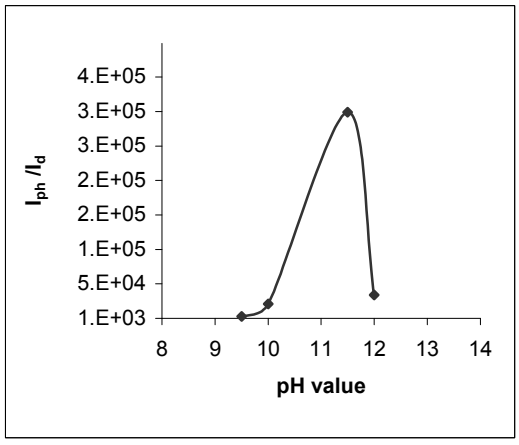

Fig. (6) Photocurrent to dark current ratio of the CdS films with pH value

The best value reported for the chemically deposited CdS films prior to our results appears to be 10^6 by Danaher et al. Even though a high

value of σ_{ph}/σ_d is not a crucial factor for solar cell applications, it is a primary requirement for photodetector applications. CdS is one of the two most sensitive photoconductors and hence it has established its place in numerous photodetecting devices [13,15].

4. Conclusions

In this paper, it was reported that the pH value of the solution has significant influences on the photoconductivity characteristics of chemically deposited CdS thin films. High quality of CdS thin films was obtained by the chemical deposition technique. It was reported that CdS films of conductivity greater than $13(\Omega.cm)^{-1}$, required for heterojunction solar cells, can be achieved without any doping. This improvement was made possible merely by varying the chemical bath parameters, so that it contains the cadmium salt and thiourea in the molar ratio 1:1.

References

[1] N.R. Pavaskar, C.A. Menezes and A.P.B. Sinha, *J. Electrochem. Soc.*, 124(5) (1977) 743-748.

[2] K.S. Ramaiah et al., *Mater. Chem. and Phys.*, 68 (1977) 22-30.

[3] T. Pisarkiewicz, E. Schabowska and E. Kusior, *J. Wide Bandgap Mater.*, 9(9) (2001) 127-132.

[4] P.K. Nair et al., *Solar Cells*, 22 (1987) 211-227.

[5] P.K. Nair and M.T.S. Nair, *Solar Cells*, 22 (1987) 103-112.

[6] S.N. Sahu and S. Chandra, *Solar Cells*, 22 (1987) 163-173.

[7] H. Metin and R. Esen, Photoconductivity studies on CdS films grown by chemical bath deposition technique, Erciyes Universitesi Fen Bilimleri Enstitusu Dergisi, 19(1-2) (2003) 96-102.

[8] I.O. Oladeji et al., *Thin Solid Films*, 359 (2000) 154-159.

[9] F.I. Ezema and P.E. Ugwuoke, *The Pacific J. Sci. & Technol.*, 5(1) (2003) 33-38.

[10] R. Grecu et al., *J. Optoelectron. Adv. Mater.*, 6(1) (2004) 127-132.

[11] W.J. Danaher, L.E. Lyons and G.C. Morris, *Solar Ener. Mater.*, 12 (1985) 137-148.

[12] J.W. Orton et al., *J. Appl. Phys.*, 53(3) (1982) 1602-1616.

[13] M.T.S. Nair, P.K. Nair and J. Campos, *Thin Solid Films*, 161(1-2) (1988) 21-34.

[14] A. Mondal, T.K. Chaudhuri and P. Pramanik, *Solar Ener. Mater.*, 7 (1983) 431-438.

[15] D. Patidar et al., *Bull. Mater. Sci.*, 29(1) (2006) 21-24.

Characterization of SiC/SiC Composites Used for Power Plant Blanket

Khalid M.Y. Hasan
Nihad I.M. El-Kashif
Salwa A.M. Ebrahim

Department of Construction Engineering, Faculty of Engineering, Zagazig University, Zagazig, Egypt

This paper describes the results of an exploratory study of blanket concepts based on SiC/SiC structure and LiPb breeder. An assessment of the performance of these concepts for advanced power plant application is presented, key issues are identified, and constraints relating to the SiC/SiC properties are discussed.

Keywords: SiC structures, Composite, Power plant, LiPb blanlet
Received: 2 November 2008, Revised: 6 December, Accepted: 11 December 2008

1. Introduction

The use of SiC/SiC composite as structural material in a fusion reactor is attractive based on its low induced radioactivity and afterheat. Several issues have been identified for the SiC/SiC material, including the cost of fabrication, the joining methods, and factors limiting the range of operation [1]. Chief among these are the rather low thermal conductivity at high temperature and under irradiation, and the maximum allowable operating temperature [2].

A liquid metal breeder provides the potential for developing a high performance, high temperature blanket system and is the breeding material of choice in this study. Two interesting candidates are LiPb and the recently proposed LiSn, both being significantly less reactive than pure Li. Both self-cooled and dual coolant options (with He as first wall coolant) are considered [3].

This paper describes the results of an exploratory study of blanket concepts based on SiC/SiC and the above liquid breeders. An assessment of the performance of these concepts for advanced power plant application is presented, key issues are identified, and constraints relating to the SiC/SiC properties are discussed. The major objective of the study is to determine the attractiveness of such a high performance blanket for an advanced fusion device and to choose the most promising concept for detailed design study.

2. SiC/SiC Parameters

Some of the major parameters influencing the attractiveness of SiC/SiC as an in-vessel structural material include: thermal conductivity; parameters limiting the temperature of operation, such as swelling under irradiation and compatibility with the liquid metal; maximum allowable stress limits; lifetime parameters; and fabrication and joining procedures [4].

Two major factors limiting the maximum operating temperature of SiC/SiC are irradiation-induced dimensional changes and compatibility with the liquid metal. Three distinct irradiation swelling temperature regimes can be identified [5,6]:

1. An amorphous phase at low temperature (<150°C) with high irradiation swelling;
2. A point defect swelling regime where swelling decreases with increasing irradiation temperature and reaches saturation at relatively low irradiation dose; and
3. A void swelling regime at high temperature where swelling keeps increasing with irradiation levels.

Clearly, the maximum SiC/SiC temperature limit must be set to avoid the void swelling regime. It is not clear at exactly what temperature the transition from point defect swelling to void swelling occurs but from the results summarized in Refs. [5] and [6], this transition temperature is about 1000°C.

The derivation of SiC/SiC stress limits for SiC/SiC was addressed as part of the ARIES-I study [1] which recommended maximum primary and secondary stress limits of 140 MPa and 190 MPa respectively (effectively based on a fraction of the computed tensile strength of 286 MPa for SiC/SiC with 60% fiber volume fraction). For the purpose of this study, these values are adopted with the understanding that they would need to be updated as improvement in the fabrication method allows for higher quality SiC/SiC material. Another factor which would need to be considered in a more detailed study is whether traditional Von Mises stress calculations are adequate or whether a new

approach should be used to account for the material orthotropy as suggested in Ref. [7].

The SiC/SiC fabrication and joining methods affect the cost of the blanket, the quality and performance of the SiC/SiC and the possibility of rejoining when replacing a component at its end of life or due to failure. Progress has been made in this area such as in the brazed joint proposed in Ref. [8]. However, much remains to be done to ensure high quality fabrication and rebonding. This study assumes that a reliable bonding method will be developed enabling one or more replacements of part of the blanket during the plant lifetime.

The SiC/SiC hermeticity issue can be mitigated by adding a SiC CVD coating to prevent leaks. In addition, the trend towards fabrication of higher quality denser multi-dimensional composite configuration should also help in minimizing any leakage. However, hermeticity should be considered as a factor when making the coolant choice in particular when this involves high pressure helium.

Table (1) summarizes the SiC/SiC properties used in this study. Note that there are other important parameters not considered within the scope of this study, such as those governing the tritium behavior, which would need to be included as part of a more detailed design study.

Table (1) SiC/SiC Properties Used in this Study

Density (kg/m^3)	3200
Density Factor	0.95
Young's Modulus (GPa)	360
Poisson's ratio	0.16
Thermal Expansion Coefficient (ppm/°C)	4.4
Thermal Conductivity in plane (W/m-K)	25
Thermal Conductivity through Thickness (W/m-K)	20
Maximum Allowable Primary Stress (MPa)	~140
Maximum Allowable Secondary Stress (MPa)	~190
Maximum Allowable Operating Temperature (°C)	1000
Max. Allowable SiC/LiPb Interface Temp. (°C)	TBD
Maximum Allowable SiC Burnup (%)	3

3. Power Cycle

The Brayton cycle offers the best near-term possibility of power conversion with high efficiency and is compatible with a high performance liquid metal blanket. For this reason, it is considered in this scoping study to evaluate the potential gain from high temperature operation with a SiC/SiC-based blanket. The Brayton cycle considered includes three-stage compression with two intercoolers and a high efficiency recuperator, as shown schematically in Fig. (1). Its main parameters are set under the assumption of state of the art components and/or with modest and reasonable extrapolation [9,10] and are as follows:

- Lowest He temperature in the cycle (heat sink) = 35 °C
- Turbine efficiency = 93%
- Compressor efficiency = 90%
- Recuperator effectiveness = 96%
- He maximum temperature <~1100°C (extrapolation required here as the range of temperature of uncooled cast nickel blades is about 850°C)
- He fractional pressure drop in out-of-vessel cycle = 0.025

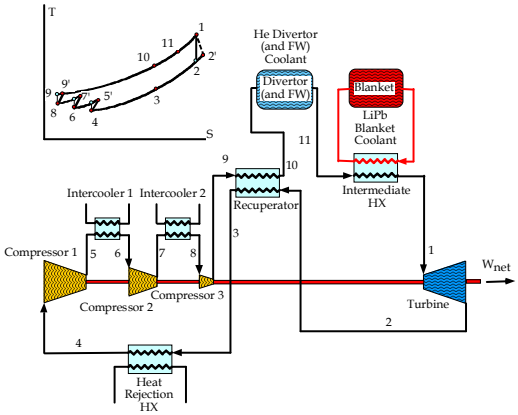

Fig. (1) Schematic of the Brayton cycle including the blanket LiPb/cycle He heat exchanger

Other parameters are set as part of the scoping parametric studies. It is assumed that the cycle He would be used to cool the divertor and first wall if applicable and would then be heated up to its maximum temperature through a heat exchange with the LiPb exiting the blanket.

4. Blanket Conceptual Study

In anticipation of the evolution of the next ARIES machine parameters based on advances in physics, superconducting magnet and technology, the power parameters assumed for the study are set to 50% higher than those of [11] while the fusion power is kept constant implying a more compact power plant. These machine and power parameters are summarized in Table (2).

Table (2) also shows some of the 3D neutronics parameters calculated for a preliminary SiC/SiC+liquid breeder design consisting of:

- A 25-cm inboard and a 55-cm outboard blanket regions with 8%SiC and 92% liquid breeder
- A 5-cm FW region on the inboard and outboard with 40% SiC and 60% liquid breeder

The resulting tritium breeding ratio was 1.1 for $Li_{17}Pb_{23}$ as breeder and only 0.95 for $Li_{25}Sn_75$ as breeder, both with 90% enriched lithium. Based on this poor breeding performance, LiSn was not considered further in this study which then concentrated solely on LiPb in a purely self-cooled configuration and in a dual-coolant configuration (He for the first wall and LiPb for the blanket).

Table (2) Machine and Power Parameters Assumed for the Study (OB=Outboard, FW=first wall)

Power Parameters	
Fusion Power (MW)	2170
Neutron Power (MW)	1736
Alpha Power (MW)	434
Current Drive Power (MW)	50
Maximum Surface Heat Flux (MW/m^2)	0.71
Average Surface Heat Flux (MW/m^2)	0.6
Power to the Divertor (MW)	140
From Neutronics Analysis	
Overall Energy Multiplication	1.1
Maximum Thermal Power (MW)	2394
Outboard Maximum Neutron Wall Load (MW/m^2)	6.6
Outboard Average Neutron Wall Load (MW/m^2)	5.6
Inboard Maximum Neutron Wall Load (MW/m^2)	5.1
Inboard Average Neutron Wall Load (MW/m^2)	3.8
OB Average Heat Generation in FW SiC (MW/m^3)	28
OB Maximum Heat Generation in FW SiC (MW/m^3)	33
OB Average Heat Generation in FW LiPb (MW/m^3)	21
OB Maximum Heat Generation in FW LiPb (MW/m^3)	25
Machine Geometry	
Major Radius (m)	4.5
Minor Radius (m)	1.13
Outboard FW Location at Midplane (m)	6
Outboard FW Location at Lower/Upper End (m)	4.5
Inboard FW Location (m)	3.5

The initial effort considered a poloidal box configuration for the blanket where the LiPb would flow in large channels whose dimensions would be set to accommodate the maximum allowable pressure and thermal stresses. In one option a separate first wall region consisting of 3-cm twisted tubes was cooled by a first LiPb pass while in the other option the first wall region was cooled by a toroidal helium flow. These two options were analyzed in some detail from which the following key points emerged for further evolving the design:

• Separate cooling of the blanket box structure with either He or an initial pass of LiPb in order to maintain the SiC/SiC within its temperature limit. The LiPb then flows in a final pass between the cooled structure and gets heated to high temperature to maximize the cycle efficiency.

• Radially segmenting the blanket in order to save on replacement cost. The first layer including the FW should be about 25 cm thick and would be replaced at the end of the FW region lifetime (about 2.8 FPY based on a 3% SiC burnup limit). The second layer would be about 35 cm thick and would be a lifetime component.

• For He, a poloidally-cooled FW configuration offers advantages of a simpler layout and manifolding configuration as well as a thinner radial build and would be preferable to a toroidally-cooled configuration.

A consistent parametric comparison between He and LiPb as poloidally-flowing first wall coolant was then performed based on parallel tube configuration schematically shown in Fig. 2. For simplicity, the minimum channel wall thickness for both cases was set as one tenth of the diameter. For the He case this would correspond to a 100 MPa pressure stress for an assumed helium pressure of 20 MPa. For the LiPb, the pressure is much lower and the assumption is more conservative.

To maximize the Brayton cycle efficiency, the LiPb exits the blanket at a high temperature of ~1150°C taking full advantage of the low velocity and low heat transfer coefficient of the final high-temperature LiPb pass to maintain the SiC/LiPb interface temperature in the higher blanket irradiation zone <~1000°. The corresponding maximum Brayton cycle He temperature in the secondary side of the heat exchanger is estimated at ~1100°C (see Fig. 1). Given this temperature and the other cycle parameters listed in the previous section the cycle efficiency would be a function of the total compression ratio and, in the case of the He-cooled first wall, of the He pressure drop in the FW channels. The compression ratio also influences the cycle helium temperature at the exit of the recuperator (point 10 in Fig. 1) which affects the first wall inlet temperature in both cases and the corresponding FW maximum SiC temperature. This is illustrated in Fig. (3) for the He-cooled first wall case.

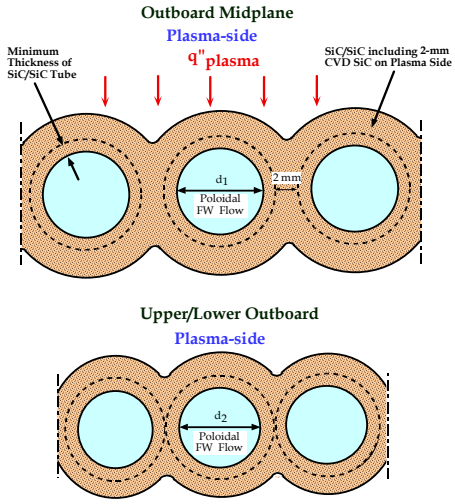

Fig. (2) Poloidally-cooled first wall configuration with tapering channels

For a given flow rate, the pressure drop would vary with the channel diameter which is shown as an alternate variable in the figure.

There is no fixed limit on the total compression ratio. Typically a higher ratio would require more stages which would drive the cost and possibly leakage rate. For a reasonable compression ratio of <3, the maximum FW SiC temperature can be maintained <1000°C for a channel diameter of 3 cm. The corresponding efficiency is ~59%.

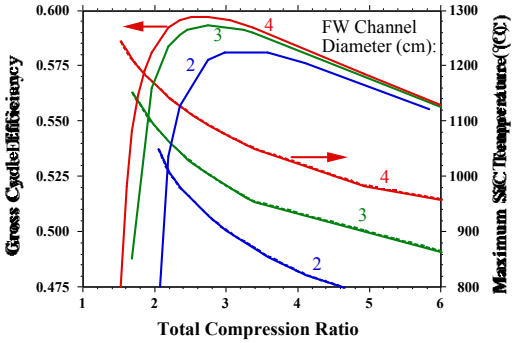

Fig. (3) Cycle efficiency and maximum SiC temperature as a function of total compression ratio for different poloidal He FW channel diameters (maximum cycle helium temperature=1100°C)

A similar analysis was done for a LiPb-cooled FW. In this case MHD effects tend to laminarize the flow even with insulated walls resulting in lower heat transfer performance and higher SiC temperature [12]. To somewhat compensate for this effect, the LiPb temperature was reduced by 50°C resulting in a maximum He cycle temperature of ~1050°C. The results are shown in Fig. 4. For a compression ratio of 3, the maximum SiC temperature is ~1000°C and the cycle efficiency ~59% for a channel diameter of 2 cm. The corresponding pressure drop including MHD effects in insulated channels [12] is relatively high, ~1.2 MPa requiring an inlet pressure of about 2 MPa.

These results are encouraging showing comparable performance for both configurations. The LiPb configuration is preferred at this stage as it helps avoid a high pressure first wall system and provides the possibility of integrating the FW and blanket without concerns about pressurizing the blanket box in case of leaks. It also provides better shielding performance in general as it also avoids any effective He "void".

5. Conclusions

This exploratory study has helped assess the potential of a SiC/SiC + LiPb blanket for a high performance blanket. High cycle efficiency can be achieved (close to 60% for the Brayton cycle) by superheating the LiPb in a final low velocity high temperature pass while maintaining the SiC/LiPb interface temperature in the irradiated blanket region within ~1000°C. This, in addition with the safety premium of using SiC/SiC makes such a concept quite attractive as a power plant blanket candidate. However, the results are dependent on the assumptions made which need to be verified through R&D. Particular areas of focus include improvement in the SiC/SiC quality and characterization of its properties at temperature and under irradiation, in particular its thermal conductivity and its compatibility with LiPb.

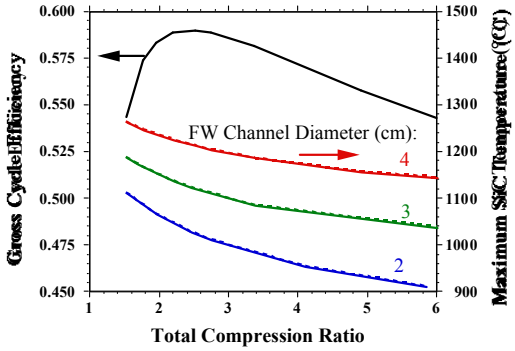

Fig. (4) Cycle efficiency and maximum SiC temperature as a function of total compression ratio for different poloidal LiPb FW channel diameters (maximum cycle He temperature=1050°C)

References

[1] F. Najmabadi, R. Conn, et al., "The ARIES-I Tokamak Reactor Study," Final Report, UCLA-PPG-1323, UCLA, CA, 1991.

[2] F. Najmabadi and R.W. Conn, "The ARIES-II and ARIES-IV Second-stability Tokamak Reactors," Proceedings TMTFE-10, La Grange Park, IL, USA, June 1992.

[3] L. Giancarli, et al., *Fusion Eng. and Design*, 41, 165- 171, 1998.

[4] S. Nishio, et al., *Fusion Eng. and Design*, 41, 357-364, 1998.

[5] S.J. Zinkle and L.L. Snead, in Fusion Materials Semiann. Prog. Rep. for period ending June 30 1998, DOE/ER-0313/24, 93-100, Oak Ridge Nat. Lab, 1998.

[6] S.J. Zinkle and L.L. Snead, in 9th Cimtec-World Forum on New Materials, Symp. VII-Innovative Materials in Advanced Energy Technologies, edited by P. Vincenzini, Techna Srl, Faenza, Italy, 307-318, 1999.

[7] S. Zinkle, *private communication*, 1999.

[8] V. Coen, et al., in High Temperature Corrosion of Technical Ceramics, Editor: R. J. Fordham, Elsevier Applied Science, London, 167-179, 1990.

[9] R. Schleicher, *private communication*, 1999.

[10] S. Malang, H. Schnauder, and M. S. Tillack, *Fusion Eng. and Design*, 41, 561-567, 1998.

[11] F. Najmabadi, and the Aries Team, *Fusion Eng. and Design*, 38, 3-25, 1997.

[12] M. A. Hoffman and G. A. Carlson, Proc. of the 13th Intersociety Energy Conversion Energy Conference SAE P-75, IEEE 78-CH1372, San Diego, August 1978.

Oday A. Hamadi
Dayah N. Raouf
Najem A. AlRubaiey

School of Applied Sciences, University of Technology, Baghdad, Iraq

Effect of Self-Absorption on the Output Power of CW CO_2 Laser

In this work, the effect of self-absorption by molecules of the active medium on the output laser power of a low-pressure CW CO_2 laser was studied. The effects of discharge current, output coupling and total gas pressure on the output laser power were discussed. It was explained that the self-absorption depends on CO_2 concentration, output coupling and discharge current and there is a threshold value for both output coupling and discharge current at which the absorption is clearly effective.

Keywords: Non-destructive test, LSAW, Ultrasonic waves, Acoustics
Received: 11 October 2008, Revised: 1 November 2008, Accepted: 8 November 2008

1. Introduction

The output power of CO_2 lasers is affected by changes may occur in the optical cavity of laser system such as scattering losses, absorption at mirror edges, diffraction losses as well as absorption by gas molecules those being heated but not excited. The unexcited CO_2 molecules inside CW laser cavity have a sever negative effect on the output power [1]. This effect is attributed to the fluctuations occuring in cavity losses resulted from several reasons, the most important one is the thermal convection originated from the self-absorption of radiation by gas molecules those heated but not electrically excited inside the cavity.

The spectral linewidth relates to the value of population inversion achieved during operation throughout its dependence on gas temperature, which determines this value as follwos [2]:

$$N = N_o \exp(-\frac{\Delta E}{K_B T}) \quad (1)$$

The instability condition in losses occurs at a certain thrshold level of output laser power. This threshold is determined by the initial state of temperature variation resulted from the rapid increase in absorption coefficient of CO_2 molecules with increasing gas temperature. Above this threshold, the output laser power is decreased with increasing losses inside the cavity due to the self-absorption by heated CO_2 molecules.

The gain coefficient (α_0) of active medium at the center of transitions band producing laser as follows [3]:

$$\alpha_o = \frac{\lambda^2}{8\pi\tau_{sp}} g(\nu_o)(N_2 - \frac{g_2}{g_1} N_1) \quad (2)$$

where λ is the wavelength, τ_{sp} is spontaneous emission lifetime, N_1 and N_2 are the population in upper and lower laser levels, respectively, g_1 and g_2 are the degeneracy of each level, respectively, $g(\nu_0)$ is the normalized gain function, which is given by:

$$g(\nu_o) = \frac{1}{8\pi\Delta\nu} \quad (3)$$

where $\Delta\nu$ is the homogenous spectral linewidth (MHz) and is a function of gas pressure (p) inside cavity and gas temperature (T), and given by [4]:

$$\Delta\nu = 7.85 p[X(CO_2) + 0.73X(N_2) + 0.6X(He)]\sqrt{\frac{300}{T}} \quad (4)$$

The homogenous spectral linewidth of laser beam related directly to the absorption coefficient of the active medium producing the laser wavelength. The absorption coefficient $\alpha_{\nu 0}(J)$ at the central frequency (ν_0) of the transition *P(20)* is given by [4]:

$$\alpha_{\nu_o}(J) = \frac{\lambda^2}{4\pi^2\Delta\nu\tau_{sp}} X(CO_2)(\frac{2J-1}{2J+1})(F^{(100)} - F^{(001)})N \quad (5)$$

where X is the partial amount of CO_2 in gas mixture, N is the total density of gas molecules, J is the rotational quantum number and $F^{(lmn)}$ is the partial fraction of the vibrational level (lmn) of the rotational quantum number J.

The attenuation resulted from the absorption of the band 10.6μm of CO_2 laser by the gas medium was studied by many published works [5-18]. These works included studying the dependences of the absorption coefficient of pure CO_2 gas as well as CO_2:N_2:He on the total gas pressure [5-6] and its temperature [7-12]. The absorption spectrum of the CO_2 laser gas medium is instrumentated by a homogenous function at total gas pressure of 10torr at the central (ν_0) of the band as given in Eq. (5).

The intracavity attenuation resulted from self-absorption by heated gas moleucles may affect

the oscillation line as the absorption coefficient $\alpha_{v0}(J)$ – depending on the rotational quantum number J – is mainly affected by gas temperature. The value of J number, at which the maxiumum value of absorption coefficient $\alpha_{v0}(J)$ is obtained, increases with gas temperature. At temperatures over 400K, the value of $\alpha_{v0}(J)$ is given by an increasing function of rotational quantum number J for J<20. Accordingly, the absorption losses due to the self-absorption is also a function of J-number and increasing within the same range.

In this work, the effect of intracavity attenuation resulted from the self-absorption by active medium molecules on the output power of homemade low-pressure CW CO_2 laser was studied and discussed.

2. Experiment

A homemade axial-flow longiturenal-discharge low-pressure CW CO_2 laser system was used in this work [19-21]. The discharge tube made of pyrex was 60cm in length and 0.8cm in diameter. In order to isolate the ZnSe front mirror from discharge region, a connection tube same as discharge tube was used but with 10cm long. The length of optical resonator was 76cm and 90cm without and with connection tube, respectivvely. The configuration of the resonator was hemispherical with a 5m-curvature gold-coated back mirror. We used four different mirrors with different transmission (40% ZnSe, 60% ZnSe, 40% Ge, 80% Ge) as the output coupler to introduce the effect of transmission on the output power.

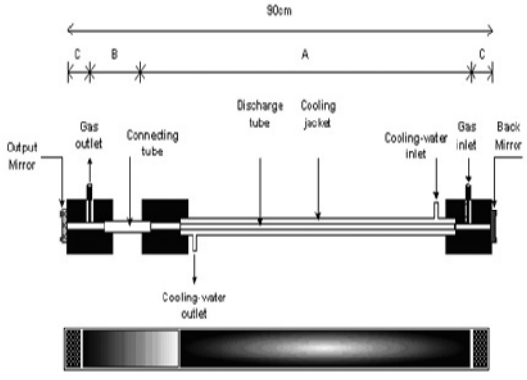

Fig. (1) Schematic diagram of the CW CO_2 laser system and the discharge regions with the intermediate connection tube

3. Results and Discussion

We consider the operation results of CW CO_2 laser system described in previous works [20-21]. They included the dependencies of output laser power on discharge current and total gas pressure inside cavity. In this work, we consider the laser system in presence of the intermediate connection tube, as shown in Fig. (1). In this case, the discharge cavity is divided into three distinct regions.

In the first region (region C), the gas is electrically excited but not cooled at both ends of the cavity. In the second region (region B), the gas is electrically excited and cooled through the gas flow along the cavity. The last one (region A) is the effective region. In region C, the self-absorption of the radiation inside cavity results in gas heating while the losses due to self-absorption in other two regions are neglegible as the gas flow rduces heating effects.

The output laser power was measured as a function of discharge current at different gas pressures inside the cavity, as shown in Fig. (2).

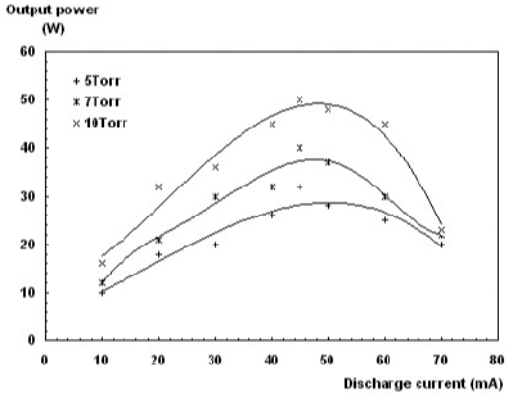

Fig. (2) Variation of output laser power with discharge current at different pressures inside laser cavity

The output power is increasing with discharge current, which represents the electrical power transferred to the gas active medium. This increasing continues to reach the maximum stability at which the maximum output laser power. The output power starts to decrease with increasing pumping power. This decrease may be attributed to the increasing heat generated from the electric discharge as the generated heat power (P_H) relates to the discharge current (I_d) by $P_H=I_d^2.R$, where R is the impedance of the gas medium.

Fig. (3) shows the variation of output laser power with the total gas pressure inside cavity at different values of discharge current. As shown, the output power increases with increasing gas pressure, which means increasing the concentration of active molecules producing laser. Due to the experimental conditions of this work, higher output power requires higher gas pressure taking into account the optimum value of discharge current, as shown in Fig. (2).

The bahavior of output power with discharge current and total gas pressure in presence of connection tube is similar to that obtained without the connection tube [20] with small difference in the optimum value of discharge current.

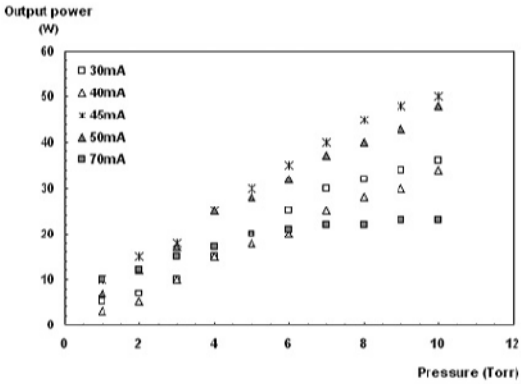

Fig. (3) Variation of output laser power with total gas pressure at different discharge currents

This similarity explains that increasing gas pressure inside cavity (or any of the three gases) leads to increase the laser output power. However, this continuous increasing – at optimum discharge current – will lead definitely to increase the spectral linewidth and hence the value of absorption coefficient (α_v) of the gaseous medium as well as decreasing the gain coefficient (α_0), according to Eq. (2) and (3). As well, reducing gas temperature leads to support the population inversion condition in the laser levels. This leads to increase the spectral linewidth and hence reducing the gain coefficient but – at the same time – reducing the absorption coefficient of the gaseous medium. As shown in Fig. (3), the optimum value of the discharge current is 45mA.

Fig. (4) shows the reasonable variation of output power with discharge current at different amounts of CO_2 in gas mixture.

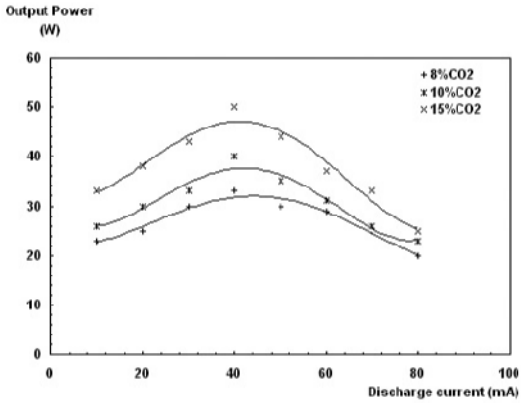

Fig. (4) Variation of output laser power with discharge current for different amounts of CO_2 pressure in the gas mixture

As the absorption coefficient of the gas mixture is proportional to the amount of CO_2, so, it can be said that the threshold condition of absorption losses, resulted from the self-absorption by active medium molecules, may be affected by the partial amount of CO_2 in gas mixture.

The output power was measured with discharge current, as shown in Fig. (5), at different values of output coupler transmission. As the output power is dependent on the transmission, then an optimum value of 60% can be determined, at which the maximum power was obtained.

Fig. (6) shows the variation of output power with total gas pressure inside cavity for two different transmission of the output coupler in two cases; using the intermediate connection tube (presence of region B) and non-using the connection tube (absence of region B).

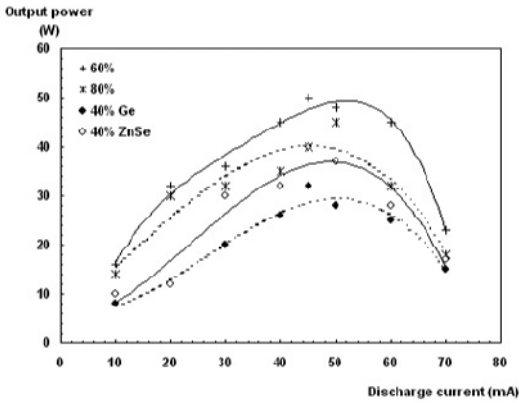

Fig. (5) Variation of output laser power with discharge current for different transmission of the output coupler at total gas pressures of 10torr

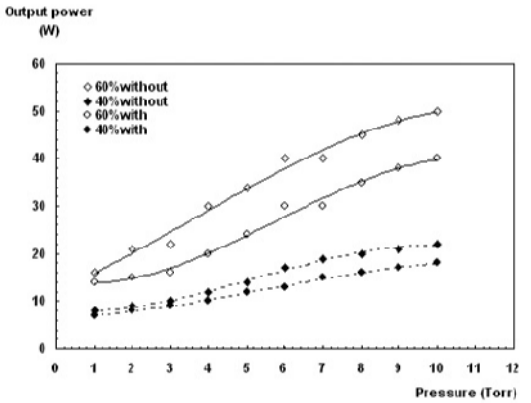

Fig. (6) Variation of output laser power with total gas pressure for two different transmission of the output coupler at the optimum discharge current in case of presence and absence of absorption losses

The presence of connection tube has an effect on output power because it creates a region inside cavity containing of gas molecules those electrically excited but not cooled because it was not surrounded by cooling water and the gas inside did not flow. In such region, the absorption coefficient (α_v) of the gas mixture is increased due to increasing gas temperature, which is originally resulted from the electric discharge. This causes an attenuation for laser radiation produced in the active region of discharge (region A) as it passes region B.

If the intracvity losses are too small, then the laser efficiency at a certain value of discharge current is dependent on gas pressure because both output power and pumping power are proportional to the gas pressure. However, all laser systems, and especially CO_2 lasers, include intracvity attenuation. Supposing intracvity losses due to attenuation resulted from the self-absorption by active medium molecules, the rate of increasing total laser efficiency is lower than the case without such losses, as shown in Fig. (7).

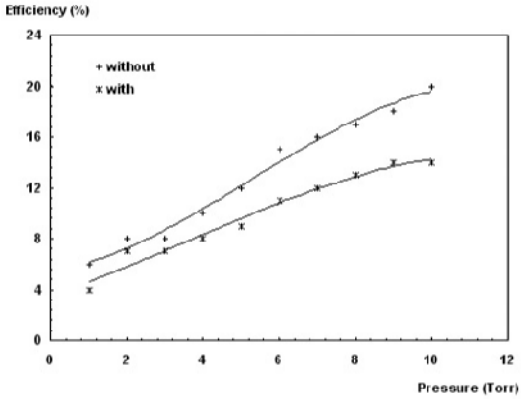

Fig. (7) Variation of total laser efficiency with total gas pressure at the optimum discharge current in case of presence and absence of absorption losses

If the gas mixture is much efficiently cooled in regions B and C throughout increasing gas flow rate or pre-cooling the gases of the mixture before feeding to the cavity, then the absorption losses can be neglected in these regions. This is attributed to the fact that the value of absorption coefficient (α_v) is too small at temperatures lower than 300K and hence the self-absorption loss can be neglected when increasing the cooling rate of gas mixture.

4. Conclusion

According to the conditions and results of this work, when the optical power absorbed by the active medium is high then the characteristics of output power are reasonably affected and the attenuation resulted from the self-absorption by active medium molecules will affect the efficiency of CW laser system. A compensation among several operation parameters, such as total gas pressure, partial amounts of gases, discharge current and output coupler transmission, is necessary to avoid the attenuation due to the self-absorption of laser radiation by the gaseous active medium itself.

References

[1] M. Hishii, et al., *Appl. Phys. Lett.,* 36 (1980) 797.
[2] C. Banwell, "**Fundamentals of Molecular Spectroscopy**", 3rd edition, McGraw-Hill Co. (London), 1983, p.25.
[3] J.T. Verdeyen, "**Laser Electronics**", Prentice-Hall, New Jersey, 1981, p.189.
[4] A. DeMaria, *IEEE Proc.,* 61 (1973) 348.
[5] T. McCubbin Jr., R. Darone and J. Sorrell, *Appl. Phys. Lett.*, 8 (1966) 118.
[6] E. Gerry and D. Leonard, *Appl. Phys. Lett.*, 8 (1966) 227.
[7] R. Ely and T. McCubbin Jr., *Appl. Opt.*, 9 (1970) 1230.
[8] S. Munjee and W. Christiansen, *Appl. Opt.*, 12 (1973) 993.
[9] R. Leonrad, *Appl. Opt.,* 13 (1974) 1920.
[10] J. Miller, *J. Appl. Phys.,* 49 (1978) 3076.
[11] A. Robinson and N. Sutton, *Appl. Opt.,* 18 (1979) 378.
[12] A. Robinson and E. Girczyc, *Appl. Opt.*, 19 (1980) 1969.
[13] M. Hishii et al., *J. Appl. Phys.,* 52 (1981) 4953.
[14] R. Brewer, C. Bruce and J. Mater, *Appl. Opt.*, 21 (1982) 4092.
[15] A. O'Keefe, J. Scherer, J. Paul and R. Saykally, "*Cavity Ringdown Laser Spectroscopy: History, Development, and Applications*", 1997, Private Communications.
[16] D.J. Knapp, "*Design and Performance of a Sealed CO_2 Laser*", 1999, Private Communications.
[17] R. Peeters, G. Berden, A. Olafsson, L. Laarhoven and G. Meijer, *Chem. Phys. Lett.*, 337 (2001) 231.
[18] B. Ullrich, R. Schroeder, W. Graupner and H. Sakai, *Opt. Express*, 9(3) (2001) 116.
[19] A.A. Ibrahim et al., *Sci. J. of IAEC,* 2(2) (2000) 100-106.
[20] N.A. Al-Rubaiey, D.N. Raouf and O.A. Hamadi, *J. Eng. Technol.*, 22(1) (2003) 1.
[21] N.A. Al-Rubaiey, D.N. Raouf and O.A. Hamadi, *Iraqi J. Laser*, 1(1) (2003) 1.

THE IRAQI JOURNAL OF APPLIED PHYSICS LETTERS
EDITORIAL BOARD

IJAPLett

COPYRIGHT RELEASE

Iraqi Journal of Applied Physics Letters (IJAPLett)

We, the undersigned, the author/authors of the article titled

……

……

……

……

that is presented to the Iraqi Journal of Applied Physics Letters (IJAPLett) for publication, declare that we have neither taken part or full text from any published work by others, nor presented or published it elsewhere in any other journal. We also declare transferring copyrights and conduct of this article to the Iraqi Journal of Applied Physics Letters (IJAPLett) after accepting it for publication.

The authors will keep the following rights:

1. **Possession of the article such as patent rights.**
2. **Free of charge use of the article or part of it in any future work by the authors such as books and lecture notes without referring to the IJAPLett.**
3. **Republishing the article for any personal purposes of the authors after taking journal permission.**

To be signed by all authors:

Signature:……..date: ……..
Printed name: ……..
Signature:……..date: ……..
Printed name: ……..
Signature:……..date: ……..
Printed name: ……..
Correspondence address:……..
……
……..
……
Telephone:……Fax:……email: ……..

Note: Please, complete and sign this form and mail it to the below address with your manuscript

The Iraqi Journal of Applied Physics Letters,

P. O. Box 55259, Baghdad 12001, IRAQ
Website: www.ijap.org, Email: ijaplett@ijap.org, ijaplett.editor@hotmail.com, Tel.: +964-7901274190

CONTENTS

VOL. 2 , NO. 1 , JANUARY-MARCH 2009

  PRINTED IN IRAQ